The Generation of EarthCARE L1 Test Data sets Using Atmospheric Model Data Sets

David P. Donovan[1], Pavlos Kollias[2,3], Almudena Velázquez Blázquez[4], and Gerd-Jan van Zadelhoff[1]

[1]Royal Netherlands Meteorological Institute (KNMI), de Bilt, the Netherlands
[2]Department of Atmospheric and Oceanic Sciences, McGill University, Quebec, Canada
[3]Division of Atmospheric Science, Stony Brook University, Stony Brook, NY, USA
[4]Royal Meteorological Institute of Belgium (RIMB), Brussels, Belgium

Correspondence: D.P. Donovan (Donovan@knmi.nl)

Abstract. The Earth Clouds and Radiation Explorer mission (EarthCARE) is a multi-instrument cloud-aerosol-radiation process study oriented mission embarking a high spectral resolution lidar, a cloud profiling radar, a multi-spectral imager and a three-view broad-band radiometer. An important aspect of the EarthCARE mission is its focus on instrument synergy. Many L2 products are the result of L1 inputs from one or more instruments. Since no existing complete observational proxy-data sets comprised of co-located and co-temporal "EarthCARE-like" data exists, it has been necessary to create synthetic data sets for the testing and development of various retrieval algorithms as well as the data processing chain. Given the synergistic nature of the processing chain, it is important that the test data are physically consistent across the various instruments. Within the EarthCARE project, a version of the EarthCARE simulator multi-instrument framework (ECSIM) has been used to create unified realistic test data frames. These simulations have been driven using high resolution atmospheric model data (described in a companion paper). In this paper, the methods used to create the test data scenes are described. As well, the simulated L1 data corresponding to each scene is presented and discussed.

1 Introduction

The Earth Clouds, Aerosol and Radiation Explorer (EarthCARE; Illingworth et al., 2015) platform comprises a 94 GHz Doppler cloud profiling radar (CPR), 355 nm high spectral resolution atmospheric lidar (ATLID), a multispectral imager (MSI), and a three–view broadband radiometer (BBR). The mission is complex in several aspects. In particular, the synergistic nature of many of the data products and the end-to-end nature of the processing chain (Eisinger et al., 2022; Barker et al., 2022) gives rise to the requirement to generate test data which is realistic and physically consistent from the point-of-view of all the instruments. For example, combined ATLID, CPR and MSI measurements will be used within the same synergistic algorithm in order to retrieve e.g. cloud particle size information. Thus, it is important, from the point of view of the various instruments, that the simulations be conducted in a physically consistent and accurate manner. Crude instrument specific parameterizations (e.g. empirical Z_e -vs- IWC relationships) should be avoided since they are not explicitly related to the basic physical atmospheric properties in a way that can be connected to the other instruments.

The requirement to generate physically consistent simulations with all of the virtual instruments "seeing" the same atmosphere in terms of both macro-and micro-physical considerations was a prime motivation in the original development of the EarthCARE simulator (ECSIM)[1] framework and its component models.

This paper first presents an overview of the ECSIM. Subsequently, the specific radiative transfer and instrument simulation methods used for each of the instruments is presented. The paper then concludes with a presentation of the simulated L1 data of the three main EarthCARE testing scenes. The input data used to build these testing scenes are described in a companion paper(Qu et al., 2022).

2   ECSIM overview

ECSIM is not a single model, but rather is a collection of tools, including radiative transfer models and instrument models, that cooperate to produce physically consistent simulations covering a range of diverse instruments.

Unlike many common radiative transfer models, ECSIM is, in principle, not tied to any particular size distribution representation. In particular, multi-wavelength, particle size resolved optical and physical characteristics (e.g. mass, maximum dimension, extinction coefficient, and phase-function) are stored in a database while the corresponding bin-resolved size distribution information is specified in separate size-distribution files. A separate master scene file stores the 3-D fields of temperature, pressure, velocity and the concentrations of relevant atmospheric gasses. This structure allows for the efficient generation of the optical properties necessary to drive diverse forward models. This process is schematically depicted in Fig.1. In the particular application described in this paper, namely the creation of test frames using Global Environmental Multi-scale (GEM) input fields as a base (Qu et al., 2022) and supplemented by aerosol data from Copernicus Atmosphere Monitoring Service (CAMS) reanalysis fields (Inness et al., 2019). The GEM and CAMS data were translated into ECSIM scene files using purpose built codes.

A key aspects of the ECSIM structure is that all the instrument simulations are driven by the same unambiguously defined atmosphere. All of the individual radiative transfer model read the same scene files and access the same scattering information data files. Whenever a model needs to calculate, for example, cloud extinction at a required wavelength, the appropriate binned size distribution (read from the scene files) is combined with the appropriate scattering properties (read from the scattering library). This structure facilitates the production of physically consistent simulations i.e. it helps insure that the models all "see the same atmospheric particles" and are "discouraged" from making their own ad-hoc assumptions regarding particle size distributions or optical/physical properties (e.g. different mass-vs-maximum dimension relationships for ice cloud particles.)

---

[1]It should be noted that The ECSIM framework was used as a basis for the development of a related framework called E3SIM. Within the context of this special issue the term E3SIM may be used in place of ECSIM. In this paper, the framework is referred to as ECSIM and the focus is not on the framework but rather the component models and methods applied to the GEM/CAMS model inputs (Qu et al., 2022) in order to generate simulated EarthCARE L1 data are described.
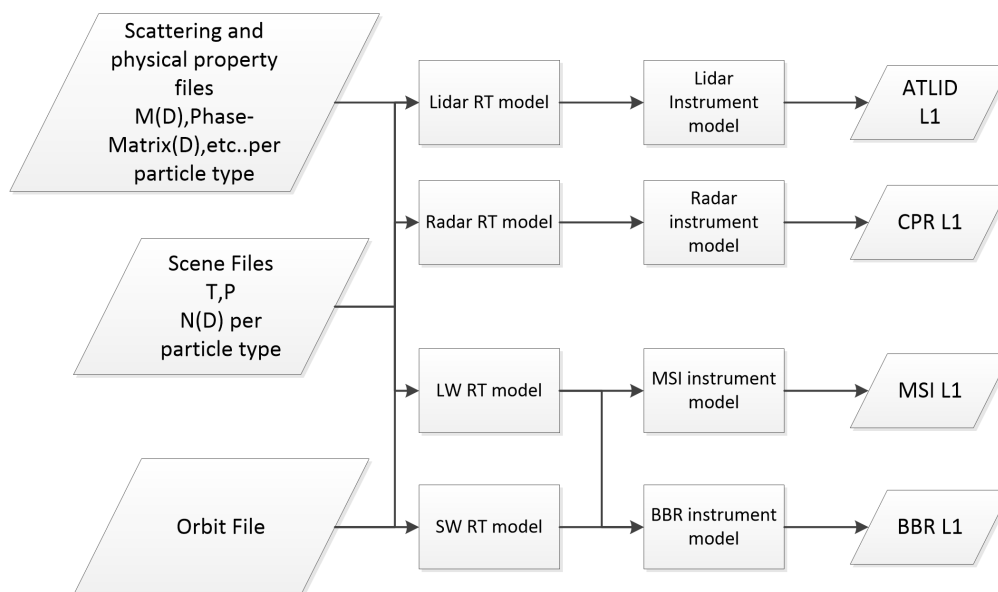
Figure 1. High level structure of ECSIM. All of the radiative transfer models read the same scene information. Another feature is that the radiative-transfer models are separate from the instrument simulation models.

2.1 Representation of the scene constituents

2.1.1 Hydrometeors

The Global Environmental Multi-scale (GEM) Numerical Weather Prediction (NWP) models runs for the EarthCARE algorithm development efforts (Qu et al., 2022) supports six different hydrometeor types: cloud droplets, raindrops, ice, snow, graupel and hail using a bin microphysical representation. The model bin microphysics scheme represents the cloud droplets particle size distribution in 50 bin sizes centered at values corresponding to cloud droplet diameters from 2 to 100 µm and the rain particle size distribution in 50 bin sizes centered at values corresponding to raindrop radius from 50 to 2500 µm. The ECCC cold microphysics scheme support four different types of particles: cloud ice, snow, graupel and hail. The particle size distribution of cloud ice is represented in 50 bin sizes centered at values corresponding to ice particle radius from 2 to 100 µm, every 2 µm. The particle size distributions of snow is represented by 100 bin sizes each from 25 to 2500 µm, every 10 µm. Table 1 summarizes the details of the bin representation of the hydrometeor species in GEM. The ice and snow hydrometeors categories have particle mass (M) and cross-sectional area (Ac) according to the Erfani and Mitchell (2016) relations for synoptic cirrus and temperatures between -40 and -20 C. The mass of the ice and snow particles in grams is given by the

3

expression $M(D) = \exp\left[a_0 + a_1 ln(D) + a_2[ln(D)]^2]\right]$, where D is in cm and the coefficients have values $a_0 = -6.72924$, $a_1 = 1.17421$ and $a_2 = -0.15980$.

Hydrometeor type	D_{min} (μm)	D_{max} (μm)	Bin spacing (μm)	Number of bins	Density (gcm^{-3})
Cloud	2	100	2	50	1.0
Rain	100	5000	100	50	1.0
Ice	4	200	4	50	(Erfani and Mitchell, 2016)
Snow	50	5000	50	100	(Erfani and Mitchell, 2016)
Graupel	100	10000	100	100	0.4
Hail	100	10000	100	100	0.9

Table 1. Cloud and precipitation microphysical parameters.

65 ### 2.1.2 VIS-UV-IR

In ECSIM, the optical scattering properties of cloud droplets and raindrops are calculated using Mie theory. The optical scattering and absorption properties of each bin are determined by averaging the scattering and absorption properties over 20 equally spaced sub-bins. Temperature dependent refractive indices were used (Hale and Querry, 1973) and calculations were done for temperatures of 240K and 300K and optical information at specific temperatures was found via interpolation.

70   For the GEM scenes, the UV-IR extinction absorption, and phase functions for ice and snow were adapted from Baum et al. (2014), using the single-particle effective radius to interpolate in particle size. Here, the effective radius is defined as

$$R_{eff}(D) = \frac{3M(D)}{4\rho_i A_c D} \tag{1}$$

where D is the particle maximum dimension, $M(D)$ is the particle mass, $A_c(D)$ is the cross-sectional area of the particle, and ρ_i is the density of solid ice. The $M(D)$ and $Ac(D)$ relationships used are described in Qu et al. (2022).

75   For both cloud-ice and snow particle types, the Baum Aggregated Solid Columns properties were used. For cloud-ice, particle maximum dimensions between 4 and 200 microns were used in steps of 4 μm. For snow, sizes between 50 and 5000 μm in steps of 25 μm. The Aggregated solid-columns phase functions generally do not have strong halo features which is in accordance with observations(Baum et al., 2014).

    The aggregated solid-columns phase functions also lack a backscatter peak, however, this is likely not in accordance with
80 observations. In particular, in Zhou and Yang (2015), the backscatter issue was investigated. They found that by directly solving Maxwell's equations numerically, a narrow backscattering peak was present for a wide range of types of ice crystals (i.e. irregular smoothed, smoothed, roughened hexagons). The width of the backscatter peak is inversely proportional to the size parameter. They also showed that accounting for this peak produces more realistic values of the lidar-ratio and improves the agreement between lidar multiple-scattering coefficients derived using Calipso observations and theory (Zhou and Yang,
85 2015).

For graupel and hail, for the UV-IR optical properties, Mie calculation were applied to equivalent effective radius spheres. This procedure produces reasonably accurate estimates of the extinction and absorption (Grenfell and Warren, 1999), however, the phase functions will not be accurate. This was not considered to be an important issue as, in the scenes considered here, occurrences of these scattering types are masked by significant amounts of cloud-ice and/or snow when viewed from above.

2.1.3 Radar

Mie scattering is used for the estimation of the backscattering and extinction coefficients for cloud droplets and raindrops. For ice and snow, the Self Similar Rayleigh-Gang Approximation (Hogan et al., 2017) is used for modelling of backscattering properties of ice and snow. The particles are assumed to be horizontally aligned with an aspect ratio of 0.6. The parameters for aggregates of bullet rosettes are as in (Hogan and Westbrook, 2014). Graupel and hail are modelled as the equal-mass spheres consisting of a blend of ice and air and using Mie theory. The dielectric properties of the mixture are calculated using Maxwell–Garnett approximation and assuming the ice inclusions in an air matrix. The gaseous attenuation is estimated using the Rosenkranz's method (Rosenkranz, 1998). The raindrops terminal velocity is estimated using (Brandes E. A. and J., 2002) and the ice and snow particles fall velocity is based on (Mitchell and Heymsfield, 2005).

2.1.4 Aerosols

The aerosol fields were constructed using CAMS aerosol component fields mapped to the following HETEAC (Wandinger et al., 2022) base component types, more detail is given in Qu et al. (2022). We reiterate here that goal of this exercise is not to produce an "optimally accurate" mapping. An ad-Hoc approximate approach in order to produce a range of "realistic enough" aerosol conditions with different optical characteristics was sufficient for the envisioned usage.

	CAMS Field				
Volume Fraction	DD1-DD3	SS1-SS2	SO4	BCB	OMB
Coarse-Dust (Spheroids)	100	9	5	3	3
Coarse non-absorbing	0	90	-0	0	0
Fine Weakly absorbing	0	1	95	0	0
Fine Strongly absorbing	0	0	0	97	97

Table 2. Mapping between CAMS aerosol components and HETEAC aerosol component types.

2.1.5 Gases

The ECSIM scenes contain the following (limited) number of gaseous species. O_2, N_2, CO_2, H_2O, O_3.

For the MSI and BBR simulations, the atmospheric transmission is calculated using a correlated-k method (Kato et al., 1999) for various narrow-bands. For each narrow-band, the aerosol and cloud optical properties are constant and represent a simple average across the band.

2.1.6 Surfaces

110 **2.1.7 SW**

For the short-wave water surfaces, the azimuth dependent BRDF for the GEM derived scenes were calculated as a function of wind-speed based on look-up tables derived from the MOMO radiative transfer model (Hollstein and Fischer, 2012) (run in unpolarized mode). The MOM ocean BRDFs (Fell and Fischer, 2001) themselves are based on a Cox-Munk approach.

For the non-snow/ice SW land surfaces, the Iso-Vol-Geo Kernel-based approach is used. For the GEM scenes, "Iso–Vol–

115 Geo" coefficients for non-ice/snow areas for a number of specific bands were supplied (Schaaf et al., 2002). The BRDFs at these bands then served as inputs to a Principle-Component based procedure for generating BRDFs for general SW frequencies Vidot and Borbáas (2014). For ice and snow surfaces, the surfaces were treated as being Lambertian with the albedo being assigned by underlying surface type (taken from the GEM model) following (Moody et al., 2007).

2.1.8 LW

120 For the Long-Wave radiative transfer calculations a much simpler approach was used. The surfaces were treated as being Lambertian and the emissivity was assumed to be a constant value of 0.93 over water and 0.98 over land.

2.2 Lidar Simulation

2.2.1 Lidar Radiative Transfer Calculations

2.2.2 Basic Considerations

125

For a single wavelength non-polarized lidar, and assuming an atmosphere the single-scattered power incident upon the detection element for a completely elastic backscatter lidar (neglecting the background signal) for a an appropriate wavelength interval centered around λ_l can be written as

$$P(z, \lambda_l) = C_{lid} z^{-2} \beta_\pi(z, \lambda_l) \exp\left[-2 \int_0^z \alpha(z', \lambda_l) dz'\right] \tag{2}$$

130 where λ_l is the laser wavelength, $P(z, \lambda_l)$ is the power the lidar will receive from a target a distance $z = ct/2$ from the lidar (where t is the elapsed time since the laser pulse was launched from the lidar), $\beta_\pi(z, \lambda_l)$ is the range and wavelength dependent backscatter coefficient in [m^{-1}sr^{-1}], $\alpha(z', \lambda_l)$ is the extinction coefficient. Here both the backscatter and extinction coefficients represent appropriate averages over the wavelength interval of interest. C_{lid} is a constant which takes into account factors related to the lidar's physical characteristics.

135 $C_{lid} = T_r E_l A_o \tag{3}$

where T_r is the bulk effective receiver transmission, E_l is the laser pulse energy and A_o is the effective receiver area.

2.2.3 Multiple-scattering

Equation 2 is valid only when single-scattering is predominant. In cases where either a high proportion of scattered photons remain within the receiver Field of View (FOV) or the optical depth is such that photon mean-free-path is small compared to the
140   instantaneous sampling volume then multiple scattering (MS) effects must be taken into account. In general, these conditions are often met for ground-based remote sensing of clouds and are always met for the case of space-based cloud remote sensing.

In order to account for multiple-scattering, the lidar radiative transfer simulations were conducted using the ECSIM-3D lidar Monte-Carlo radiative transfer code. The approach used is described within (Donovan et al., 2015) and additional relevant detail, not covered within Donovan et al. (2015) is given here. In particular, the approach used to determine the spectral
145   properties of the return signal is discussed. Within the MS model, each photon packet is assigned both a mean relative spectral shift (initially zero) from its center wavelengths and a Gaussian spectral width. The Doppler shift of the packets is calculated according to the relative velocity of the scatterers encountered and the scattering geometry. The spectral width is initialised using the laser line-width and is hardly affected by particulate scattering but can be substantially widened if molecular scattering has occurred.

150   2.2.4 Doppler shift and Multiple Scattering

Even neglecting such processes involving the change of energy levels within the target scatterers (i.e. rotational–vibrational Raman scattering, fluorescence etc.) the scattered radiation will be Doppler shifted according to the relative motion of the scatterers with respect to the lidar. In general, a target moving with respect to a fixed lidar will 'see' a source whose frequency is given by (neglecting terms of order $(v/c)^2$)

$$155 \quad f = f_o \left(1 + \frac{v}{c} \cos(\theta) \right) \tag{4}$$

where v is the velocity of the scatterer, c is the speed of light, θ is the angle between the scatterers velocity vector and the line-of-sight directed back toward the receiver, and f_o is the frequency of the source light in the frame of the laser. When light initially incident upon the moving scatterer, is scattered, it is equivalent to being instantaneously absorbed and re-emitted so that the scattered light will again be Doppler shifted in frequency depending on the motion of the scatterer with respect to the
160   receiver. Accordingly, the frequency measured by an observer in the same frame as the lidar transmitter will be given by (again neglecting terms of order $(v/c)^2$)

$$f = f_o \left[1 + \frac{v}{c} \left(\cos(\theta) + \cos(\theta_{sc}) \right) \right] \tag{5}$$

where θ_{sc} is the angle between the velocity vector and the scattered photon's trajectory. So that light scattered directly forward and measured by a stationary observer would have no Doppler shift while light scattered directly backwards to the

165 lidar would be observed to have been shifted in wavelength by an amount twice that predicted by Eq. 4 Thus even if the laser line width was infinitely narrow the return would still be broadened due to the motion of the scatterers relative to the lidar.
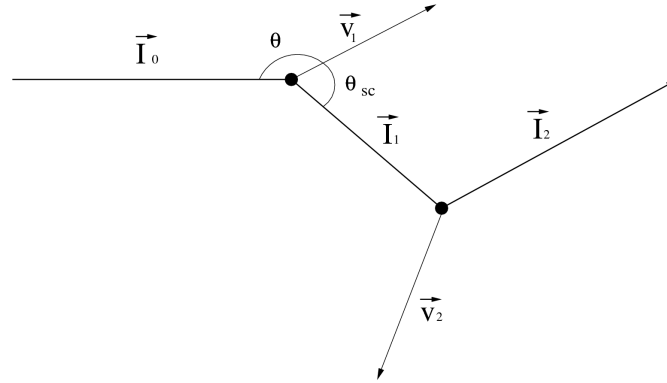

Figure 2. Geometry relevant for determining the observed Doppler shift after multiple scatters.

The occurrence of multiple scattering will have implications with respect to the spectral signature of the lidar return. By repeated application of Eq. 4 (see Fig. 2) it can be shown that the Doppler shifted frequency measured by an observer in the same frame as the lidar after n scatters will be given by

$$170 \quad f_n = f_o \left(1 + \frac{1}{c} (\mathbf{v}_1 \cdot \mathbf{I}_0 + (\mathbf{v}_1 - \mathbf{v}_2) \cdot \mathbf{I}_1 + (\mathbf{v}_2 - \mathbf{v}_3) \cdot \mathbf{I}_2 + \cdots \mathbf{v}_n \cdot \mathbf{I}_n) \right) \tag{6}$$

where $\mathbf{v}_i$ is the velocity vector of the ith scatterer and $\mathbf{I}_i$ is the unit vector for the photon trajectory for the ith scatter. If the lidar is to observe the photon, to a good approximation, it must be scattered directly backwards towards the lidar receiver so that $\mathbf{I_n} = -\mathbf{I_o}$ and thus,

$$f_n = f_o \left(1 + \frac{1}{c} (\mathbf{v}_1 \cdot \mathbf{I}_0 + (\mathbf{v}_1 - \mathbf{v}_2) \cdot \mathbf{I}_1 + (\mathbf{v}_2 - \mathbf{v}_3) \cdot \mathbf{I}_2 + \cdots - \mathbf{v}_n \cdot \mathbf{I}_o) \right) \tag{7}$$

175 **2.2.5 Spectral Broadening and Multiple-scattering**

In the MC model the spectral width of the packets is also tracked. The width is initialized using the laser spectral line width. The Gaussian width after subsequent scattering events is calculated by convolving the spectral witdh of the incoming packet with the spectral width induced by the scattering event (accounting the scattering geometry). For particulate scattering, the spectral width is assumed to be unaffected. However, for molecular scattering events thermal broadening is important. How

180 this is modelled in ECSIM is described in the following subsection.
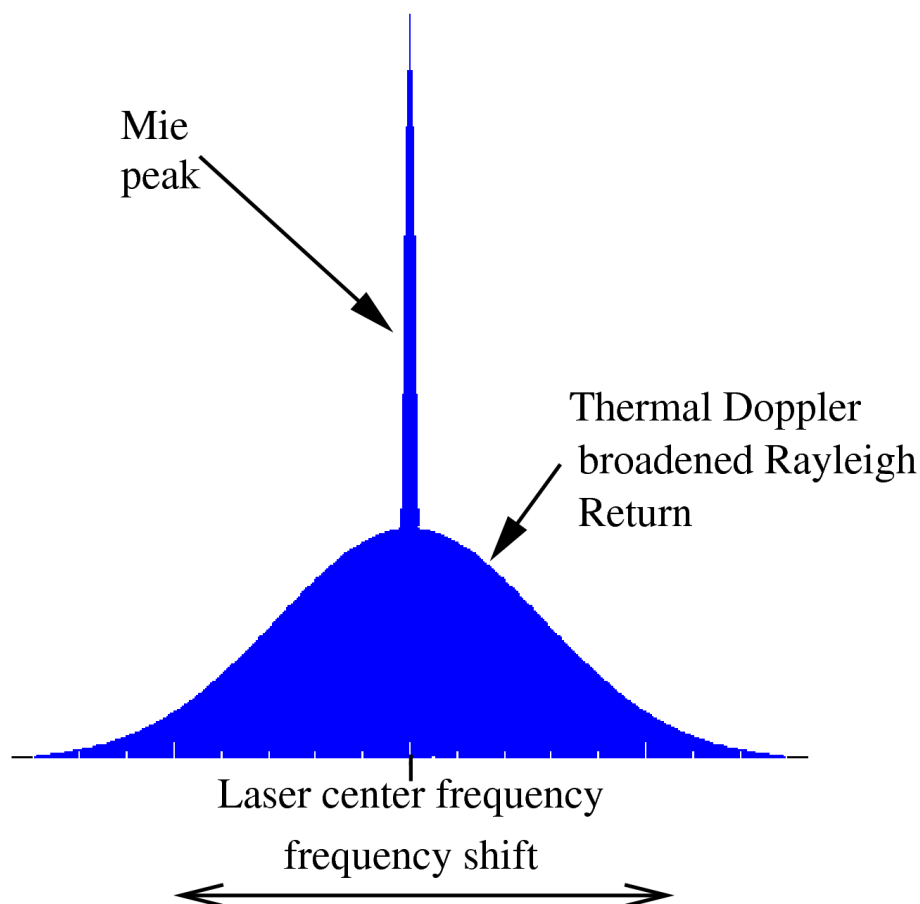
Figure 3. Idealized view of spectral signature of a lidar return.

2.2.6 Rayleigh-Brillouin Scattering

A schematic representation of the spectral signature of a general lidar return signal is shown in Fig. 3 The spectral width of the particulate backscattering peak will be determined by the spectral width of the laser pulse itself along with any turbulence present in the sampling volume. The spectral width of the laser will be on the order of $10^{-7}f_o$, so that the laser line width will usually be the dominant factor. The molecular backscatter though will be much broader than the particulate scattering return; this is due to the fact that the atmospheric molecules have a large thermal velocity. For low densities the Half-Maximum Half Width (HMHW) of the broadening produced by the thermal motions alone is given by

$$\Delta f = f_o \left(\frac{8kT\log(2)}{Mc^2} \right) \tag{8}$$

9

where, k is Boltzmann's constant, M is the average molecular mass, and T is temperature. For typical values of atmospheric
temperature the HMHW of the Doppler return will be on the order of $4 \times 10^{-6} f_o$ so that the Doppler broadening will be 10-20
greater than the laser line width. Eq. 8 applies at low gas densities.

In general, the central (non-Raman) Rayleigh line profile (Cabannes line) will consist of three components, a central peak
together with two flanking "Brillouin-Mandel'shtam" peaks (Miles et al., 2001). In the low density or high temperature regimes
the uncorrelated motion of the scatterers gives rise to a Gaussian velocity distribution centered around the mean velocity of the
flow and Eq. 8 applies. As the pressure increases or the temperature decreases, density fluctuations on the order of the laser
wavelength may appear. These density fluctuations travel at the speed of sound in the gas and will give rise to acoustic side
bands.

The Rayleigh-Brillouin scattering line shape may be quantified in terms of the so-called y parameter which is defined in
terms of the ratio of the laser wavelength to the mean free-path. For the Earth's atmosphere

$$y = 0.230 \left[\frac{T + 111}{T^2} \right] \left[\frac{P\lambda}{\sin(\frac{\theta}{2})} \right] \tag{9}$$

here T is the temperature in Kelvin, P is the pressure in atmospheres, λ is the laser wavelength and θ is the scattering angle.
Here x is a normalized frequency parameter defined as

$$x = \frac{\sqrt{2}\lambda}{4\sin\left(\frac{\theta}{2}\right)} \left(\frac{\nu}{\nu_o} \right) \tag{10}$$

where μ is the frequency shift from the line center and ν_o is the sound-speed

$$\nu_o = \sqrt{\frac{kT}{m}} \tag{11}$$

where m is the molecular mass.

For low y parameters, the lineshape has a simple Gaussian form. For larger values of y (in the range that we must be
concerned with) the line shape becomes complicated and somewhat costly to evaluate. Fortunately, for values of y under
about 10 the Rayleigh-Brillouin line shape may be accurately enough (for our purposes) approximated by the sum of three
independent Gaussian functions.

For the single-scatter return the line shape is determined by the sum of three Gaussian profiles. These calculations are based
on the results of pre-computed approximate Gaussian fits made to accurate calculations of the line profile (Pan et al., 2002)
corresponding to various y parameters (See Fig. 4). For the higher order scattering, at each molecular scattering event the
probability of the scattered photon packet being shifted to one of the acoustic side bands is calculated. Whether or not the
center frequency of the photon packet is shifted is then determined stochasticly using the relative weights of the component
Gaussians and the subsequent shift and width of the associated Gaussian profile is used to determine the line shape. This line
shape and shift is then used in the subsequent for the next multiple-scattering scattering event.
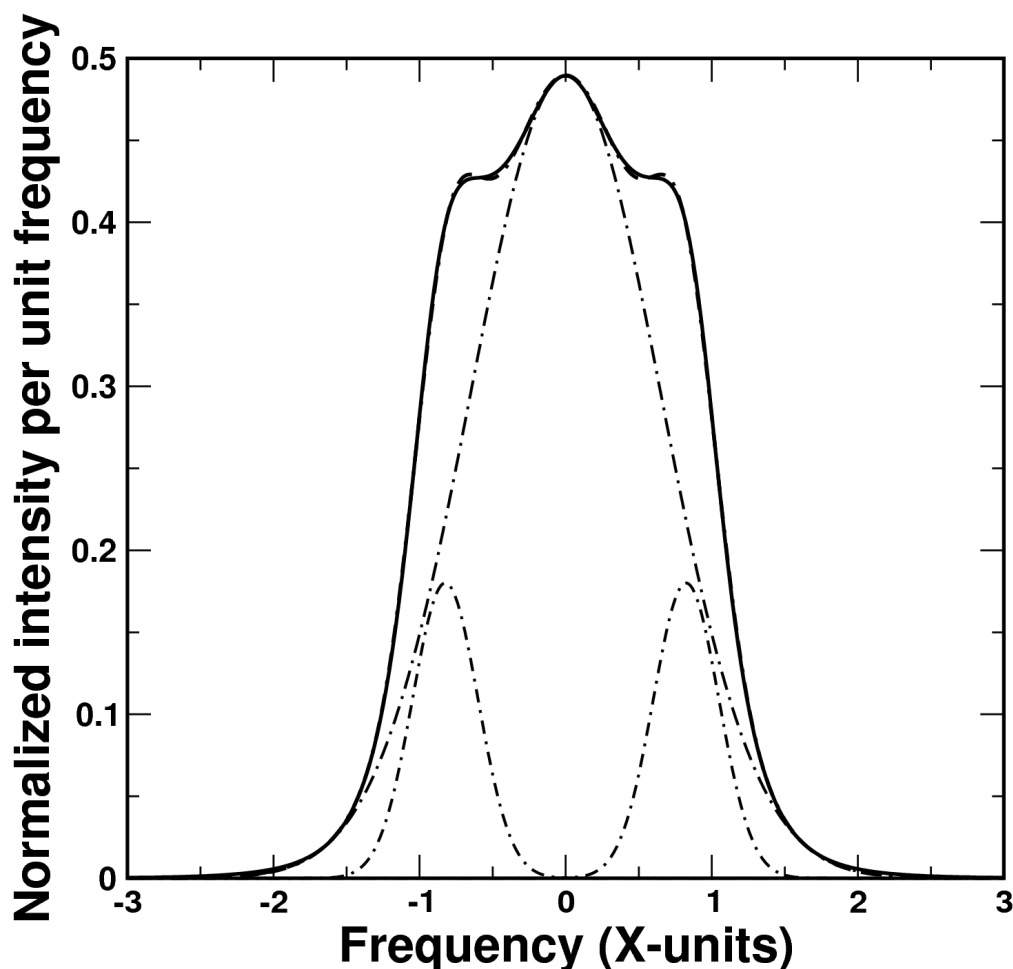
Figure 4. Exact Rayleigh-Brillouin line shape (Solid-Line) along with fitted sum of three Gaussian functions (Dashed–Dotted–line). The three component Gaussian functions are also shown. Here the y parameter is equal to 1.0.

2.2.7 Lidar Instrument Model

ATLID possesses three receiver channels. A co-polar, so-called "Mie" channel which detects mainly particulate (i.e. clouds and aerosol) backscatter, a co-polar, so-called "Rayleigh" channel which detects mainly backscatter from molecules, and a cross-polar particulate+molecular channel. The Mie-Rayleigh separation is achieved using a Fabry-Perot Etalon. For details of ATLID's design see do Carmo et al. (2016) and do Carmo et al. (2021). Some of the important ATLID technical specifications are repeated in Table 3.

The ECSIM lidar instrument model ingests the output of the the lidar radiative transfer model and models the instrument response function including instrument noise. The model is capable of being configured to simulate various lidars, in this case ATLID. The instrument model process the time-spectral-polarization resolved output of the lidar radiative transfer model and

Parameter	Value
Telescope Diameter (m)	0.62
Wavelength (nm)	355
Receiver field-of-view (full-angle) (mads)	66.5
Laser Divergence (full-angle) (mrads)	36
Pulse Energy (mJ)	35
Range resolution (m)	100m (0-20km)/500m(20km–40)km
PRF (Hz)	51
End-of-Life Co-polar-Mie transmission	45
End-of-Life Co-polar-Mie transmission	43
End-of-Life Co-polar-Mie transmission	43
Quantum Efficiency	79/75/79
Molecular backscatter in Mie co-polar channel fraction	25 %
Mie backscatter in Rayleigh co-polar channel fraction	16 %

Table 3. CPR Technical Specifications

includes explicit modelling of the Fabry-Perot Etalon HSRL spectrometer as well as the effects of the background filter etc. Poisson shot noise is simulated as are the effects of dark-current, solar background and ACCD read-out-noise.

2.2.8 Background Signal

230 The background signal refers to power registered by the lidar receiver that is due to the detection of photons from sources other than backscattered laser light. In the case here, the main source of background light will be scattered sunlight from the Earth's surface and atmosphere. As such, the background will depend on the solar angle, the surface type and the cloud cover. In this work, the lidar background values were based on an approximate look-up-table approach where the background irradiance at 355 nm was modelled using a radiative model for various cloud optical depths, surface albedos and solar zenith angle.

235 The background power incident upon the detector level is given by:

$$P_{back} = A_o \pi \rho_t \overline{I_b(\lambda) T_{rec}(\lambda)} \Delta\lambda \tag{12}$$

where A_o is the effective receiver area, ρ_t is the telescope $^1\!/_2$ angle field-of-view, and $\overline{I_b(\lambda) T_{rec}(\lambda)}$ is the average product of the receiver wavelength dependent transmission (including filtering) with the up-welling irradiance, and $\Delta\lambda$ is the wavelength interval that must be considered.

240 ### 2.2.9 Receiver Optical Elements

The ATLID lidar receiver optical train is modelled as a sequence of elements that operate on the spectral and polarization state of the lidar return. For simplicity, it is assumed that the polarization elements (i.e. beam splitters, horizontal and vertical linear

polarizers, half-wave plates etc..) act perfectly in polarization space (but, however, may have a non-ideal intensity efficiency)
while broad-band spectral filters were modeled as having a rectangular passbands and are characterized by a single in-band
245 transmission/reflection and a out-of-band reflection/transmission pair.

The Fabry-Perot (FP) etalon is the most critical optical element in ATLID's receiver chain. This element is used to separate
the Mie signal from the Rayleigh signal.

The transmission function of an etalon without accounting for non-ideal effects such as the finite input beam collimation and
surface roughness may be modeled (Saleh and Teich, 1991) as

$$250 \quad T = \left(1 - \frac{A}{1-R}\right) \times \frac{1}{1 + \frac{4R}{(1-R)^2}\sin^2\frac{\delta}{2}} \tag{13}$$

where R is the reflection coefficient of the etalon mirrors, A is the relative absorption and scattering loss parameter and
$\delta = 2\pi\frac{\lambda-\lambda_o}{\lambda_o}$ where λ_o is the central wavelength. The corresponding etalon reflection function may be written as:

$$R = \frac{(1.0 - R - A)^2}{1.0 - 2.0 * R * cos(\phi) + R^2}. \tag{14}$$

The effects of non-parallel mirror flatness, diffraction and non-ideal beam collimation are taken into account by convolving the
255 above absorbing etalon transmission and reflection functions by a top-hat function whose width in wavenumbers is given by:

$$\Delta\nu_{total} = \sqrt{\Delta\nu_{np}^2 + \Delta\nu_{ap}^2 + \Delta\nu_{dif}^2} \tag{15}$$

where $\Delta\nu_{np}$ accounts for the broadening due to non-parallel mirror alignment, $\Delta\nu_{ap}$ accounts for columation or finite aperture
effects

$$\Delta\nu_{ap} = 1.0 - \cos\left[\left(\frac{D_t}{D_{fp}}\right)^2 \frac{\rho_t}{2}\right] \tag{16}$$

260 where D_t is the telescope diameter, D_{fp} is the etalon diameter and ρ_t is the telescope full-angle field-of-view in radians. $\Delta\nu_{dif}$
accounts for diffraction effects and is given by:

$$\Delta\nu_{dif} = 1.0 - \cos\left[\left(\frac{\lambda_o}{D_t}\right)\right] \tag{17}$$

An example etalon transmission and reflection profile as a function of $\nu - \nu_o$ is shown in Fig. 5. Here $T = 0.978$, $A = 0.0$,
the Free-spectral-range (the distance between adjacent transmission maximums) is 0.5 cm^{-1}, the flatness parameter is $\lambda_o/300$,
265 the telescope fov is 5×10^{-3} mrads, the telescope diameter is 0.6 m and the etalon diameter is 0.05 m.

2.2.10 Noise Considerations

For a given time interval, the number of photons arriving at a given detector channel is given by

$$N_{det} = \frac{\lambda_o}{hc}(P_{lid} + P_{back})\Delta t \tag{18}$$
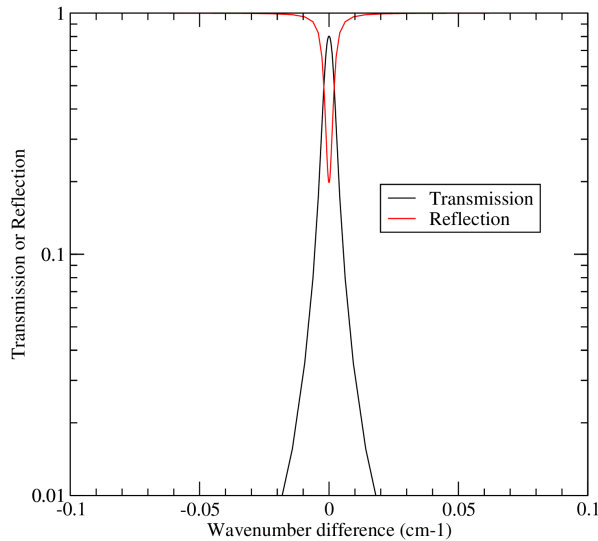
Figure 5. Etalon reflection and transmission showing non-ideal behavior.

where Δt is the averaging time interval, h is Planck's constant, λ_o is an appropriate mean wavelength for the detector channel in question , P_{lid} is the power received from the lidar and P_{back} is the background power arising from the up-welling reflected solar radiance at 355 nm. According to Poisson statistics the standard deviation of N_{det}, shot-noise, is simply given by

$$\delta N_{det} = \sqrt{N_{det}} \tag{19}$$

In addition to the shot-noise, the effects of dark current noise and ACCD readout noise are also simulated.

2.2.11 Spectral cross-talk

The characteristics of the HSRL filter ensure that a degree of spectral cross-talk between the Mie and Rayleigh channels exists (do Carmo et al., 2021). The effects of cross-talk are simulated within the lidar instrument model. The lidar instrument model also applies a cross-talk correction, following the ATLID L0 to L1 processor step. This correction assumes perfect knowledge of the appropriate cross-talk coefficients. In flight, uncertainties in the coefficients will introduce additional errors, however, this is not envisioned to be a significant issue as the in-flight values of the coefficients are envisioned to be known within an accuracy of a few percent. This is to be achieved using a combination of a priori on ground characterization as well as in flight monitoring and adjustment e.g. using returns above 35 km (where only molecular scattering returns should be expected) to quantify the amount of Rayleigh-to-Mie cross-talk and using ground and suitably thick clouds returns (where to a good

approximation only elastic particulate scattering returns should be expected) to quantify the Mie-to-Rayleigh cross talk. Due to the occurrence of variable but possibly significant amounts of molecular Brillouin scattering in liquid water (Hostetler et al., 2018), water surfaces are not expected to be suitable cross-talk coefficient determination targets for ATLID.

2.3 Radar Simulation

2.3.1 Radar Radiative Transfer Calculations

The radar scattering calculations described in Section 2 are used to estimate the radar backscatter cross section $\sigma_{b,j}(D)$ for each hydrometeor species j and particle maximum diameter D in units of m. In addition, the extinction cross-section $\sigma_{e,j}(D)$ for each hydrometeor species j and particle maximum diameter D is estimated in units of m^2. The GEM particle size distribution number concentration $n_j(D)$ is provided in units of m^{-3} (integrated across the bin diameter width) and the particle sedimentation velocity $V_j(D)$ is provided in units of ms^{-1}.

Thus, the radar reflectivity factor Z_e ($mm^6 m^{-3}$), specific attenuation A ($dBkm^{-1}$) and reflectivity-weighted hydrometeor sedimentation velocity V_{SED} (ms^{-1}) are estimated for each hydrometeor species as follows:

$$Z_{e,j} = 10^{18} \frac{\lambda^4}{\pi^5 |K_w} | \sum_{i=1}^{Nbins} [\sigma_{b,j}(D) \, n_j(D)] \tag{20}$$

$$A_j = \frac{0.01}{\ln(10)} \sum_{i=1}^{Nbins} [\sigma_{e,j}(D) \, n_j(D)] \tag{21}$$

$$V_{SED,j} = \frac{\sum_{i=1}^{Nbins} [\sigma_{b,j}(D) \, n_j(D) \, V_j(D)]}{\sum_{i=1}^{Nbins} [\sigma_{b,j}(D) \, n_j(D)]} \tag{22}$$

where λ is the wavelength in m, j is the index for the hydrometeor species (cloud, rain, ice, snow, graupel and hail) and $|K_w^2|$ is the dielectric factor of water at 94-GHz. The aforementioned parameters are combined to produce their total value at each GEM grid point

$$Z_e = \sum_{i=1}^{6} Z_{e,j} \qquad A_h = \sum_{i=1}^{6} A_j \qquad V_{SED} = \frac{\sum_{i=1}^{6} [Z_{e,j} \, V_{SED,j}]}{Z_e} \tag{23}$$

The effect of water vapor on measured CPR reflectivity can be significant. For example, two-way attenuation from surface to upper troposphere of more than 5 dB is not unusual in tropics. Josset et al. (2013) compared different models to estimate absorption at W-band by gases by taking advantage of the collocated CloudSat–Cloud-Aerosol Lidar and Infrared Pathfinder Satellite Observation (CALIPSO) measurements. Their results indicate that the Rosenkranz (1998) model fits the observations best. The nadir o-way gaseous attenuation α_g from space is calculated using Rosenkranz (1998) and the water vapor mixing ratio profile from the X-MET product (Eisinger et al., 2022).

Finally, the normalized (per unit of area) cross section of the Earth's surface σ_0 $[m^{-1}]$is estimated. Over an ocean surface, the normalized cross section is estimated using the relationship from Li et al. (2015) as a function of the near surface wind

310 speed provided in the X-MET data product. CloudSat observations have shown that over the ocean surface σ_0 is known within 2 dB (Tanelli et al., 2008) and over land exhibits very large variability due to its dependency on vegetation, surface slope, soil moisture, snow cover and other factors (Haynes et al., 2009). At 94-GHz, the ocean surface σ_0 varies between 16 to 6 dB for near surface wind speeds between 2 to 20 ms^{-1} respectively (Tanelli et al., 2008). The corresponding radar reflectivity factor for the Earth's surface is estimated using the formula:

315 $$Z_{SFC} = 10^{18} \frac{\sigma_0 \lambda^4}{\pi^5 |K_w|^2 \Delta Z} \tag{24}$$

where ΔZ is the EarthCARE CPR range resolution (500 m).

2.3.2 Radar Instrument Model

The EarthCARE CPR instrument model has two main modules. The first is the sampling geometry module that determines which part of the GEM model is sampled by the CPR at any given time step (or along track location) and accounts also for the

320 along track displacement of the satellite sampling volume during signal integration. The second module is the CPR receiver module that introduces the instrument noise and estimates the CPR Doppler moments and their corresponding uncertainty (Kollias et al., 2007, 2022b). Some of the important EarthCARE CPR technical specifications are shown in Table 4.

Parameter	Value
Antenna Diameter (m)	2.5
Frequency (GHz)	94.05
Noise ($mm^6 m^{-3}$)	0.0071
Altitude (km)	400
Pulse Length (m)	500
Range resolution (m)	100
Min Range (km)	-1
Max Range (km)	20
PRF (Hz)	6100 - 7500
Speed (ms^{-1})	7600
Altitude (km)	400
θ_{3dB} (deg)	0.095
IFOV$_{3dB}$ (m)	700

Table 4. CPR Technical Specifications

Following (Kollias et al., 2014, 2022b) the antenna weighting function $W_a(x,y)$ is shown in Fig. 6 where x and y are the along and cross track dimensions respectively. The $W_a(x,y)$ determines the contribution of GEM model grid point radar reflectivity $Z_e(x,y)$ to the total radar reflectivity observed by the CPR at a particular model grid. At a GEM model height z, the radar reflectivity contribution $Z_{GEM}(z)$ to the CPR is estimated using the equation:

$$Z_{GEM}(z) = \sum_{i=1}^{Xbins} \sum_{j=1}^{Ybins} [Z_e(i,j) \, W_a(i,j)] \tag{25}$$

where $Xbins$ and $Ybins$ are the number of GEM grid points that are illuminated by the CPR radiation. Next, the CPR range weighting function $W_r(x,y)$ that described the along range point target response of a radar is applied to estimate CPR measured radar reflectivity at a particular range r. The CPR range weighting function for the EarthCARE and CloudSat CPR's are shown in Fig. 6.
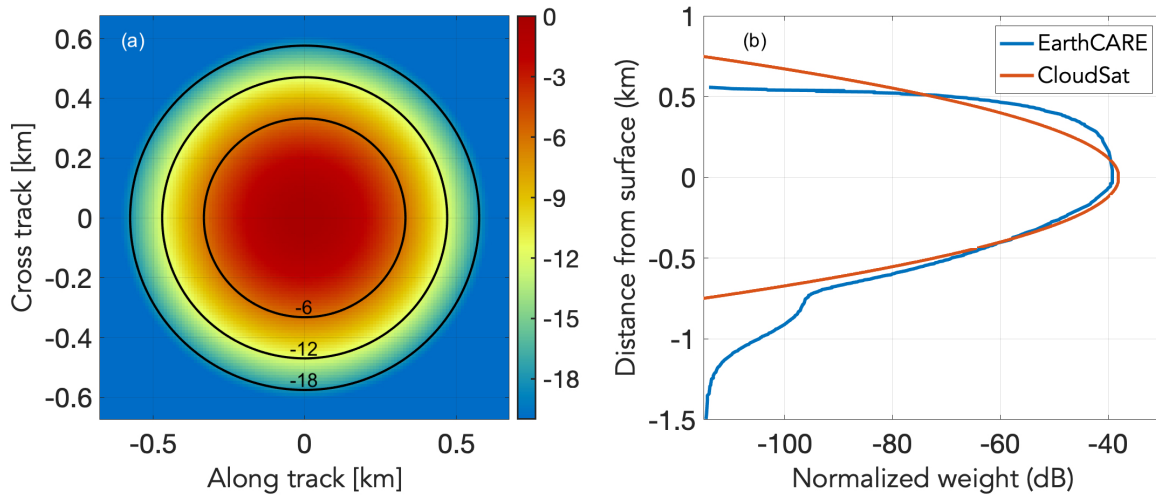
Figure 6. (a)the EarthCARE CPR antenna weighting function $W_a(x,y)$ distributions in the along and cross track direction. Units are dB below the peak value. (b) The range weighting function $W_r(x,y)$ for CloudSat and EarthCARE

The CPR range weighting function is the result of the transmitted waveform (the same for both radar) and the CPR receiver filter. The EarthCARE CPR receiver filter was designed to sharply cut off the $W_r(x,y)$ at 500 m above the Earth's surface to improve the detection of low-level clouds compare to CloudSat (Lamer et al., 2020). The CPR radar reflectivity at range r is estimated using the equation:

$$Z_{CPR}(r) = \sum_{i=1}^{Gbins} [Z_{GEM}(z(i) - r) \, W_r(z(i) - r)] \tag{26}$$

where $Gbins$ is the number of GEM model levels within the limits of the CPR range weighting function centered at range r. The forward simulation of the EarthCARE CPR Doppler velocity and spectrum width requires to introduce the apparent Doppler velocity $V_{app}(x)$ introduced to each GEM model point within the CPR footprint will have due to the satellite motion

340   V_{sat}. The $V_{app}(x)$ is estimated using the equation:

$$V_{app}(x) = -x \frac{V_{sat}}{H_{sat}} \tag{27}$$

where x is the distance from nadir and H_{sat} is the altitude of the satellite Fig. 7. The $V_{app}(x)$ is independent of the cross-track distance y, thus $V_{app}(x,y) = V_{app}(x)$. At a GEM model height z, the Doppler velocity contribution $V_{GEM}(z)$ to the CPR is estimated using the equation:

345   $$V_{GEM}(z) = \sum_{i=1}^{Xbins} \sum_{j=1}^{Ybins} [Z_e(i,j) \, W_a(i,j) \, (V_{app}(i,j) + W_{air}(i,j) + V_{SED}(i,j))] \tag{28}$$

where $W_{air}(i,j)$ is the vertical air motion (negative is up) and $V_{SED}(i,j)$ is the total sedimentation velocity at the (i,j) GEM grid point.

In the CPR receiver module, the product $S_v(i,j) = Z_e(i,j)W_a(i,j)$ and the sum of all the velocity components $V_{tol}(i,j) = V_{app}(i,j) + W_{air}(i,j) + V_{SED}(i,j)$ are used to construct the periodogram $S(V)$ $(mm^6 m^{-3}/ms^{-1})$ of the returned radar signal at each height z of the GEM model following the methodology proposed first by (Zrnic, 1975). Since we are using radar

350   reflectivity at power, the noise is also given in radar reflectivity units (see Table 3). The periodogram is a very useful tool for describing a time series data set. In a radar system, the PRF determines the temporal resolution of the time series data at a particular range gate. The periodogram is an estimate of the spectral density of a signal. The periodogram is interpolated at a spectral velocity resolution that is determined by the CPR sampling rate (PRF) which determines the higher sampled frequency.

355   This is often called Nyquist frequency ($F_N = PRF/2$), which is half the sampling frequency of a discrete signal processing system. It is sometimes known as the folding frequency of a sampling system. Using the radar wavelength λ (Table 3), we can convert the folding frequency to folding velocity or as often-called Nyquist velocity ($V_N = PRF\lambda/4$). If the Doppler velocity of a radar target exceeds the magnitude of the Nyquist velocity, folding occurs (aliasing).

Once the radar receiver noise is added in the frequency domain, the next step is to perform Inverse Fast Fourier Trans-

360   form (IFFT) of the constructed Doppler spectrum in order to retrieve I (in-phase) and Q (quadrature-phase) voltage time series (Kollias et al., 2014). The in-phase channel includes the portion of the signal in phase with the reference sinusoid. The quadrature-phase channel includes the portion of the signal 90° out of phase with the reference sinusoid, is abbreviated Q The IFFT operator is applied to the amplitude spectrum. The temporal spacing of the I/Q voltages is $1/PRF$. As described in (Kollias et al., 2014), the I/Q time series at each GEM model height z are convoluted along range with the square root of

365   the range weighting function $W_r(x,y)$ and then are used as input to a pulse-pair Doppler moments estimator (Zrnic, 1977) to provide estimates of the CPR radar reflectivity, Doppler velocity and Doppler spectrum width.
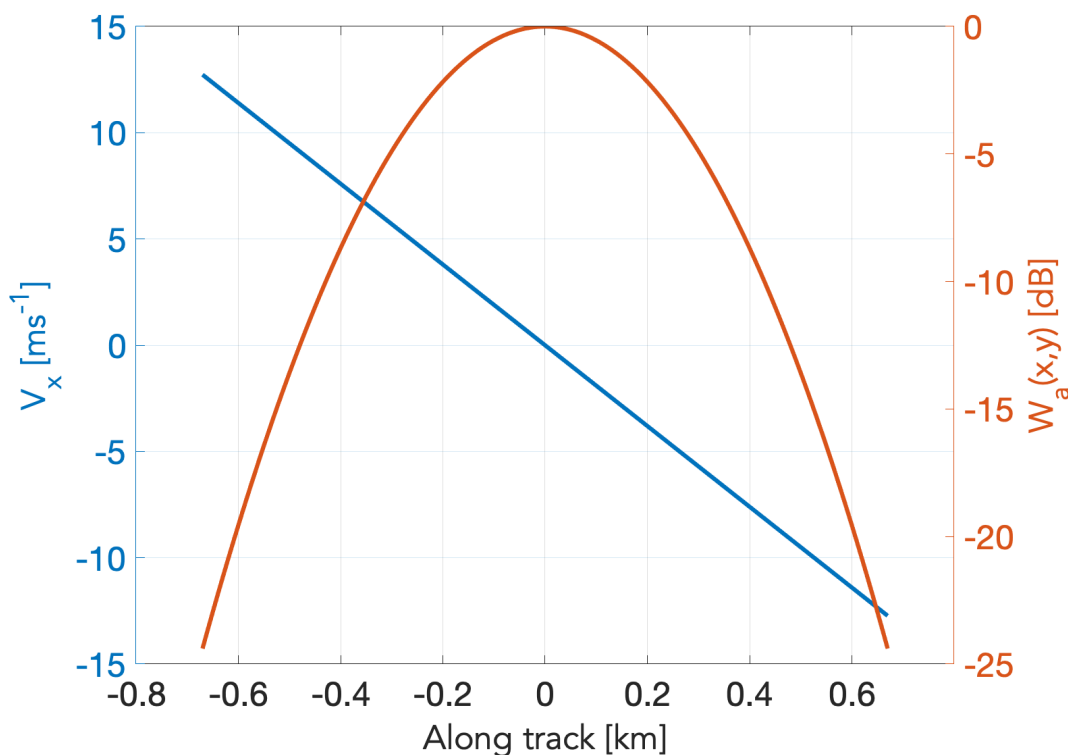
Figure 7. The EarthCARE CPR antenna weighting function $W_a(x,y)$ and apparent Doppler velocity $V_{app}(x)$ distribution as a function of distance in the along track direction

2.4 MSI Simulation

2.4.1 Short-Wave Radiative transfer Calculations

The short-wave radiances for the first four MSI channels were performed by applying a one dimension radiative transfer model.
370 ECSIM contains an option to perform 3D Monte-Carlo calculations, however, it was unfeasible to apply this option for the totality of the domain required. The 1D calculations used DISORT with 32 streams (Lin et al., 2015) driven by the atmospheric absorption, phase functions, and surface BRDFs extracted from the scene file. The band-limits and relevant atmospheric gasses for the MSI SW bands are listed in Table 5, here for simplicity, a top-hat response was assumed. The MSI retrieval algorithms make this same assumptions when applied to the simulated data, however, the detailed non-ideal spectral response of each
375 channel will be full accounted for when these algorithms are supplied with actual observations.

Even with a 1-D approach, the computation covering the 6000-by-150 km frame domain at a horizontal resolution of 0.25 km is computationally demanding. In order to speed-up the process, a sampling and interpolation process was implemented as follows,

1. The domain was divided into a number of sub-domains of n×m pixels. In this work n=12 and m=12.

2. For each pixel in the sub-domain the quantities $X_1(i,j) = A_s(i,j)\exp(-tau(i,j))$ and $X_2(i,j) = \exp(-tau(i,j))$ were calculated, where τ is the particulate optical depth and A_s is the pixel black-sky albedo.

3. Within each subdomain the pixels where DISORT would be applied to were selected accordingly,

   (a) The lower left pixels were selected by default

   (b) In the along-track direction each ith and jth pixels are selected by default. In this work, every 5th pixel was used.

   (c) The pixels along the spacecraft nadir track are selected by default.

   (d) The pixels with the maximum and minimum values of X_1 and X_2 respectively and selected.

4. For each of the selected pixels, DISORT is used to calculate the TOA radiances.

5. For each of the non-selected pixels (denoted by i_n,j_n) the radiance of the selected pixels (i_s,j_s) are scanned through and the pixel that minimizes $abs(X_1(i_n,j_n) - (X_1(i_s,j_s) + abs(X_2(i_n,j_n) - (X_2(i_s,j_s))$ is used to fill in the TOA radiance.

6. The domain was shifted by half its width in the along-track direction and then shifted in the cross-track direction when the end of the frame was reached and the process repeated until the entire frame was covered. The overlap between domains was found to be useful for eliminating artifacts mimicking the sub-domain structure.

The procedure was able to speed-up the necessary calculation by an order of magnitude while retaining a suitable degree of accuracy. This is mainly due to the high degree of correlation in the clouds fields for distances less than 1.5 km or so. This echos the findings of Barker and Li (2019).

After the MSI short-wave calculations were performed (at a resolution of 0.25 km), the radiances were binned to the MSI instrument resolution (1-km) and the effects of instrument random noise was simulated using a Gaussian pseudo-random number generator. Technical details of the MSI can be found in Chang (2019).

Channel	v_1 cm^{-1}	v_2 cm^{-1}	Gasses
MSI_1 660 nm	14948.	15408.	H_2O, O_3
MSI_2 865 nm	11429.	11696.	H_2O
MSI_3 1.61 um	6098.	6329.	CO_2
MSI_4 2.2 um	4444.	4651.	H_2O, CH_4

Table 5. Short-wave Multispectral Imager (MSI) bands.

2.4.2 Long-Wave Radiative transfer Calculations

400 Like the short-wave msi calculations, the TOA radiances for the long-wave MSI channels (see Table 6) were calculated using DISORT. Since the long-wave calculations are not as computationally demanding as the short-wave calculations, no sampling strategy was necessary and DISORT with 16 streams specified was applied to every pixel in the MSI frame domain.

As was the case with the short–wave channels, the idealized radiances at 0.25 km resolution were binned to the MSI instrument resolution (1-km) and the effects of instrument random noise was simulated using a Gaussian pseudo-random number
405 generator.

Channel	v_1 cm^{-1}	v_2 cm^{-1}	Gasses
MSI_5 8.85 μm	1064.	1205.	H_2O, O_3
MSI_6 10.85 μm	885.	962.	H_2O, O_3
MSI_7 11.85 μm	813.	877.	H_2O, CO_2

Table 6. Long-wave multispectral imager (MSI) Bands.

2.5 BBR Simulation

The methods described for the MSI short and long–wave TOA radiances were applied to the BBR calculations for the spectral-band resolved BBR TOA radiances for each of the three BBR views as well as the TOA fluxes. The short-wave bands used are listed in Table 7 and long-wave bands are listed in Table 8.

Broad-Band Short Wave 0.2-4.0 μ m							
Center λ	Gasses	**Center** λ	Gasses	**Center** λ	Gasses	**Center** λ	Gasses
0.254998	O_3	0.277389	O_3	0.294507	O_3	0.317148	O_3
0.344614	O_3	0.384187	O_3	0.428872	O_3	0.482614	O_3
0.528597	O_3	0.544707	H_2O	0.557927	O_3	0.585172	H_2O O_3
0.614836	O_3	0.645182	H_2O O_3	0.675333	O_3	0.694179	H_2O O_3 O_2
0.723040,	H_2O	0.766254	O_2	0.817094	H_2O	0.866138	H_2O
0.929973	H_2O	1.00908	H_2O	1.11501	H_2O	1.33592	H_2O
1.56311	H_2O CO_2	1.77179	H_2O	2.05465	H_2O CO_2	2.21263	H_2O
2.58866	H_2O CO_2	3.28839	H_2O O_3	3.80445	H_2O CO_2	4.27991	H_2O CO_2

Table 7. Center wavelengths used for broad-band short-wave calculations and relevant gasses.

410 The BBR ideal radiances at 250m resolution as calculated by the radiative transfer code were used to create simulated L1-b data, i.e, BBR filtered radiances: B-NOM, and BBR single pixel filtered radiances: B-SNG (see production model in

Long-Wave 4.0-400.0 μ m									
Center λ	Gasses	**Center λ**	Gasses	**Center λ**	Gasses	**Center λ**	Gasses	**Center λ**	Gasses
4.07997	H_2O	4.23729	H_2O	4.38596	H_2O	4.54545	H_2O	4.71698	H_2O
4.90196	H_2O	5.02513	H_2O	5.07614	H_2O	5.12820	H_2O	5.18135	H_2O
5.23560	H_2O	5.29101	H_2O	5.34759	H_2O	5.40541	H_2O	5.46448	H_2O
5.52486	H_2O	5.58659	H_2O	5.64972	H_2O	5.71429	H_2O	5.78035	H_2O
5.84795	H_2O	5.91716	H_2O	5.98802	H_2O	6.06061	H_2O	6.13497	H_2O
6.21118	H_2O	6.28931	H_2O	6.36943	H_2O	6.45161	H_2O	6.53595	H_2O
6.62252	H_2O	6.71141	H_2O	6.80272	H_2O	6.89655	H_2O	6.99301	H_2O
7.09220	H_2O	7.19424	H_2O	7.29927	H_2O	7.40741	H_2O	7.51880	H_2O
7.63359	H_2O	7.75194	H_2O	7.87402	H_2O O_3	8.00000	H_2O O_3	8.13008	H_2O O_3
8.26446	H_2O O_3	8.40336	H_2O O_3	8.54701	H_2O O_3	8.69565	H_2O O_3	8.84956	H_2O O_3
9.00901	H_2O O_3	9.17431	H_2O O_3	9.34579	H_2O O_3	9.52381	H_2O O_3	9.70874	H_2O O_3
9.90099	H_2O O_3	10.1010	H_2O O_3	10.3093	H_2O O_3	10.5263	H_2O O_3	10.7527	H_2O O_3
10.9890	H_2O O_3	11.2360	H_2O	11.4943	H_2O	11.7647	H_2O	12.0482	H_2O CO_2
12.3457	H_2O CO_2	12.6582	H_2O CO_2	12.9870	H_2O CO_2	13.3333	H_2O CO_2	13.6986	H_2O CO_2
14.0845	H_2O CO_2	14.4928	H_2O CO_2	14.9254	H_2O CO_2	15.3846	H_2O CO_2	15.8730	H_2O CO_2
16.3934	H_2O CO_2	16.9492	H_2O CO_2	17.5439	H_2O CO_2	18.1818	H_2O CO_2	18.8679	H_2O CO_2
19.6078	H_2O CO_2	20.4082	H_2O	21.2766	H_2O	22.2222	H_2O	23.2558	H_2O
24.3902	H_2O	25.6410	H_2O	27.0270	H_2O	28.5714	H_2O	30.3030	H_2O
32.2581	H_2O	34.4828	H_2O	37.0370	H_2O	40.0000	H_2O	43.4783	H_2O
47.6190	H_2O	52.6316	H_2O	58.8235	H_2O	66.6667	H_2O	76.9231	H_2O
90.9091	H_2O	111.111	H_2O	142.857	H_2O	200.000	H_2O	333.333	H_2O

Table 8. Center wavelengths used for broad-band long-wave calculations and relevant gasses.

Eisinger et al. (2022)). This process involved in a first step the convolution of the simulated radiances with the spectral responses of the BBR instrument to obtain Broadband SW, L_{SW}, and LW, L_{LW}, radiances at 250m. Secondly, as the BBR instrument will measure TW radiances, which are not simulated, the TW (L_{TW}) radiances at 250m resolutions are calculated as $L_{TW} = L_{LW} + A \cdot L_{SW}$ (Velázquez-Blázquez et al., 2022). In order to simulate realistic L1 B-SNG inputs, the Chopper Drum Mechanism (CDM) speed has to be taken into account. It has been configured at a 0.7 ratio of the original nominal speed, as recommended to maximise the lifetime of the mechanism, which defines a ground sampling distance for two consecutive SW or TW measurements of 1.1 km. The current BBR simulator software to produce the B-SNG input performs a bilinear interpolation of the 250m broadband radiances at the positions of the 30 detectors array and this for each of the BBR views (fore, nadir and aft). The resulting B-SNG SW and TW radiances for the Halifax scenes are show in Figures 8 and 9. Finally, a

domain integration or psf-weighting is done to pass from the single pixel radiances in B-SNG to the nominal BBR resolutions in B-NOM (standard, full and small), sampled every 1km.
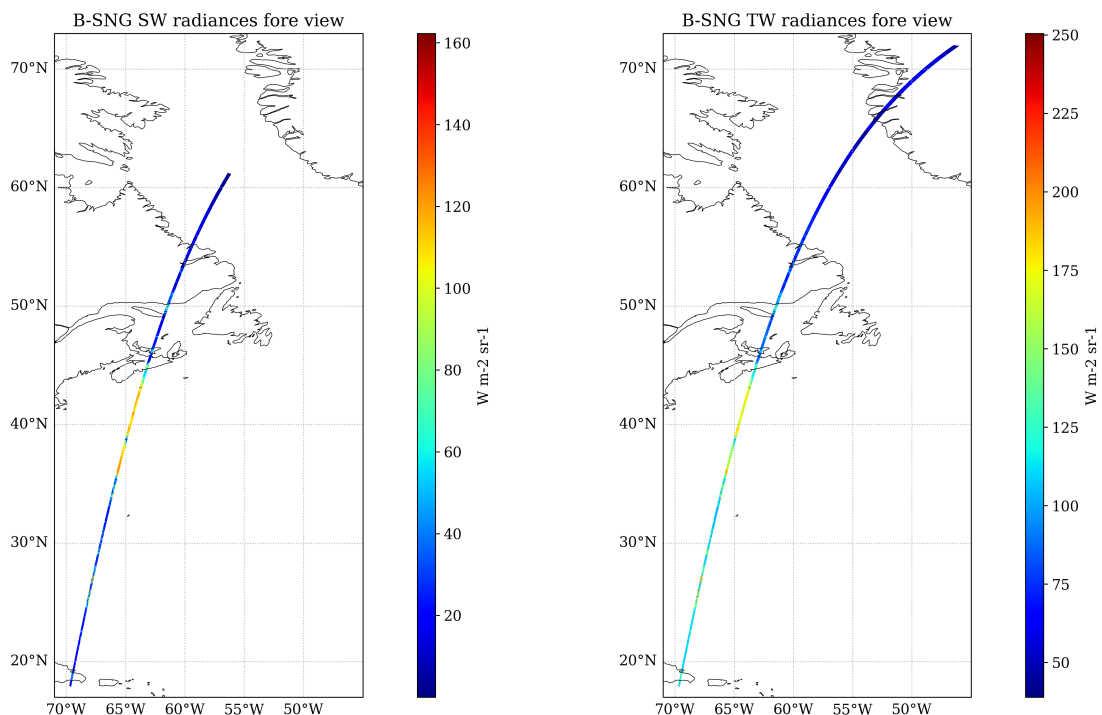

Figure 8. Simulated B-SNG TOA broadband radiances for the fore view of the BBR SW and TW channels for the Halifax scene. Similar plots are obtained for the nadir and aft view

3 The Tests Frames

In this section, simulated L1 data for the EarthCARE test scenes are presented and discussed. The Level-11 simulated data as well as various model truth fields for 3 GEM derived scenes are available in the available from https://doi.org/10.5281/zenodo.7117115. The GEM data is discussed in Qu et al. (2022).

3.1 Halifax

The high-latitude part of the Halifax scene features mixed-phase clouds at night-time, transitioning from deeper clouds with tops up to 6 km around 65°N featuring supercooled liquid in convective cells, to mixed-phase clouds with tops around 3 km
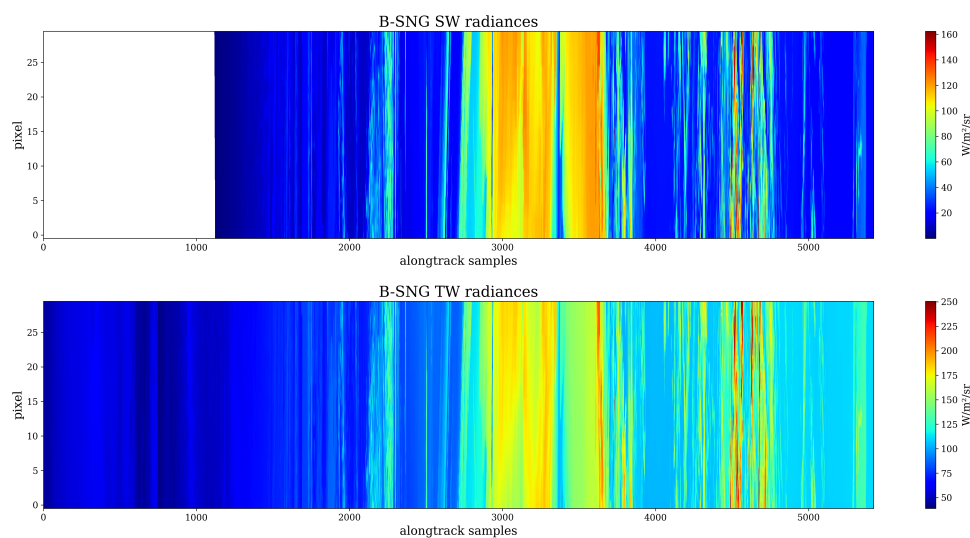
Figure 9. Simulated B-SNG TOA broadband radiances for the for view of the BBR SW and TW channels for the Halifax scene.

430   at temperatures as cold as $-30°$C, and finally to more broken shallow mixed-phase clouds toward $50°$N. Near the center of the frame a storm system with supercooled layers, convective precipitation and ice clouds with tops up to altitudes of 13 km are present. South of about $45°N$ cloud-free and shallow low altitude water clouds are present. Also south of $45°N$ there are extended aerosol regions present. From the ground to above 2 km a marine layer (mainly Sea-Salt) is present with above a thinner continental pollution layer (mainly fine-mode non absorbing aerosol). The differences in the lidar ratio associated with
435   these two aerosol regions shown in the middle panel of Figure 10 is evident.

     The simulated ATLID Mie, Rayleigh and Cross-polar attenuated backscattters are shown in Figure 11. It can be seen that, as expected, the lidar penetration into the clouds is limited, especially in the central part of the frame. However, most of the ice clouds are well captured. The aerosol fields in the southern segment of the frame are also well captured.

     The nadir fields of particle mass, effective radius, and simulated observed Radar reflectivity for the full Halifax scene are
440   shown in Figure 12. The 'striped' area in the radar reflectivity present in the upper-left of the lowers panel is due to a simulated change in maximum height covered by the radar which is associated with a latitude dependent change in the operating PRF. Radar reflectivity is a strong function of the particle effective radius, hence, in general, the larger effective radii regions of the scene are well sampled, while areas containing relativity small water cloud droplets are not.

     The GEM model and CPR simulated signals for a selected region of the Halifax scene are shown in 13. Due to the large
445   horizontal extend of the scene, we focus on the $[30° - 48°N]$ simulated region that covers the frontal and convective systems. The top two panels shows the unattenuated 94-GHz radar reflectivity and the reflectivity weighted hydrometeor sedimentation velocity at the GEM grid resolution. The two systems are characterized by high cloud tops ($12km$), periods with thick high level clouds and extensive periods with light and moderate precipitation. The lower two panels show the raw (uncorrected) CPR radar reflectivity and mean Doppler velocity measurements. The EarthCARE CPR has sufficient sensitivity to detect the
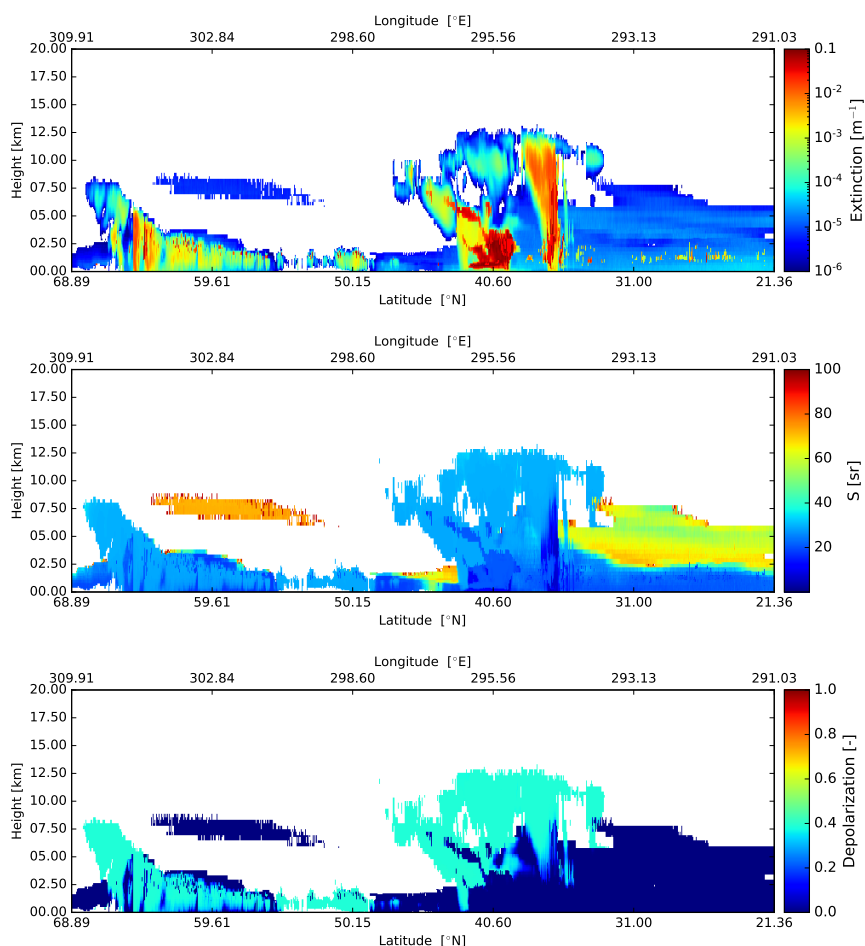
Figure 10. Cross-sections of the extinction at 355 nm, lidar extinction-to-backscatter ratio, and linear depolarization ratio, following the simulated EarthCARE orbit for the Halifax scene

450 hydrometeor layers except weak reflectivity echoes near the highest cloud tops. The strong 94-GHz attenuation by hydrometeors results to missed detections near the surface. This can be clearly seen by the depression of the surface echo radar reflectivity at 3700 km and the complete loss of the surface echo around 4100 km. The fainted CPR echoes that fill the surface echo gap around 4100 km are due to multiple scattering (Battaglia et al., 2010). As expected, the CPR raw Doppler velocity field (500 m along track integration) is noisy (Kollias et al., 2014, 2022a). The post-processing algorithm described in (Kollias et al.,

455 2022b) are expected to significantly improve the quality of the CPR Doppler velocity measurements. Despite their noisiness, the CPR Doppler velocities reproduce the main features of the GEM model Doppler velocities, namely, the transition from solid to liquid hydrometeors and the low sedimentation Doppler velocities in the upper cloud levels.
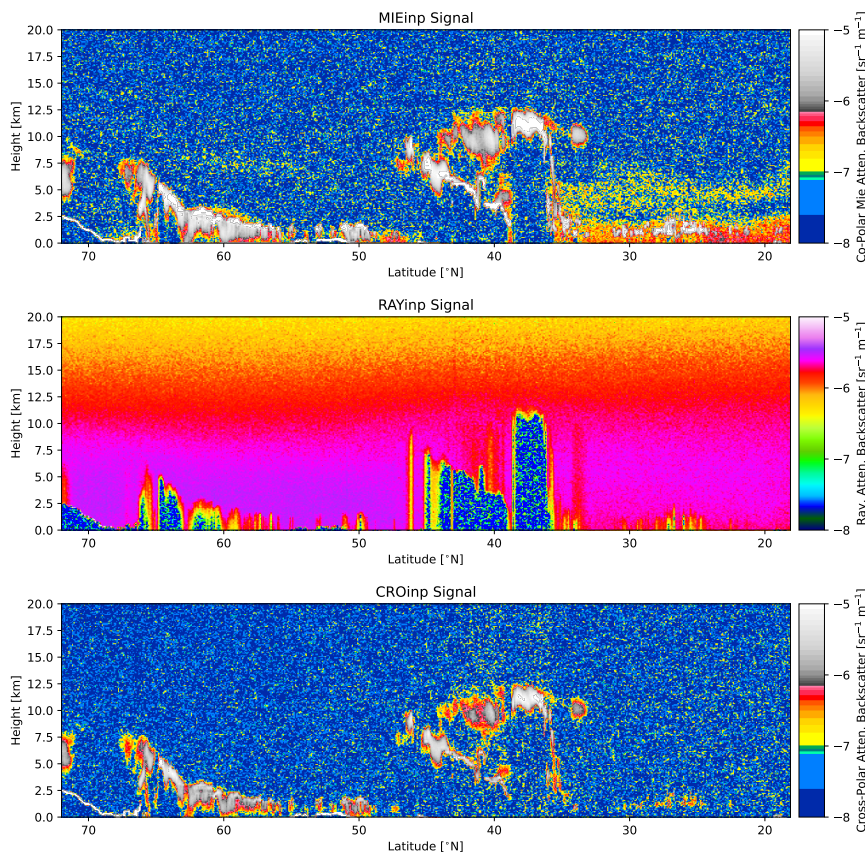
Figure 11. Simulated Mie channel, Rayleigh channel, and Cross-Polar ATLID attenuated backscatters for the Halifax scene.

The simulated short-wave TOA radiances for the MSI short-wave channels are shown in Figure 14. Here, north of about 55°N, the sun is below the horizon so that the radiances are zero. Below about 42°N the swath is above ocean with the exception of passing over the Dominican Republic near the southern frame border.

The simulated long-wave TOA brightness temperatures for the MSI long-wave channels are shown in Fig. 16. Here it can be seen that cold (but low altitude) clouds tops north of 55° N are visible, as are the cold (but high) cloud top temperatures between 35°N and 45°N. The warm land and ocean temperatures are also apparent in the mainly cloud-free region south of about 35° N. A close-up of the channel 1 radiances for the Halifax scene between 32.5°N and 37.5°N can be seen within Fig. 17

The NDVI (defined as the difference in reflectances divided by their sum for the two indicated channels) fields corresponding to the radiances shown in Fig. 14 are shown in Fig. 15.
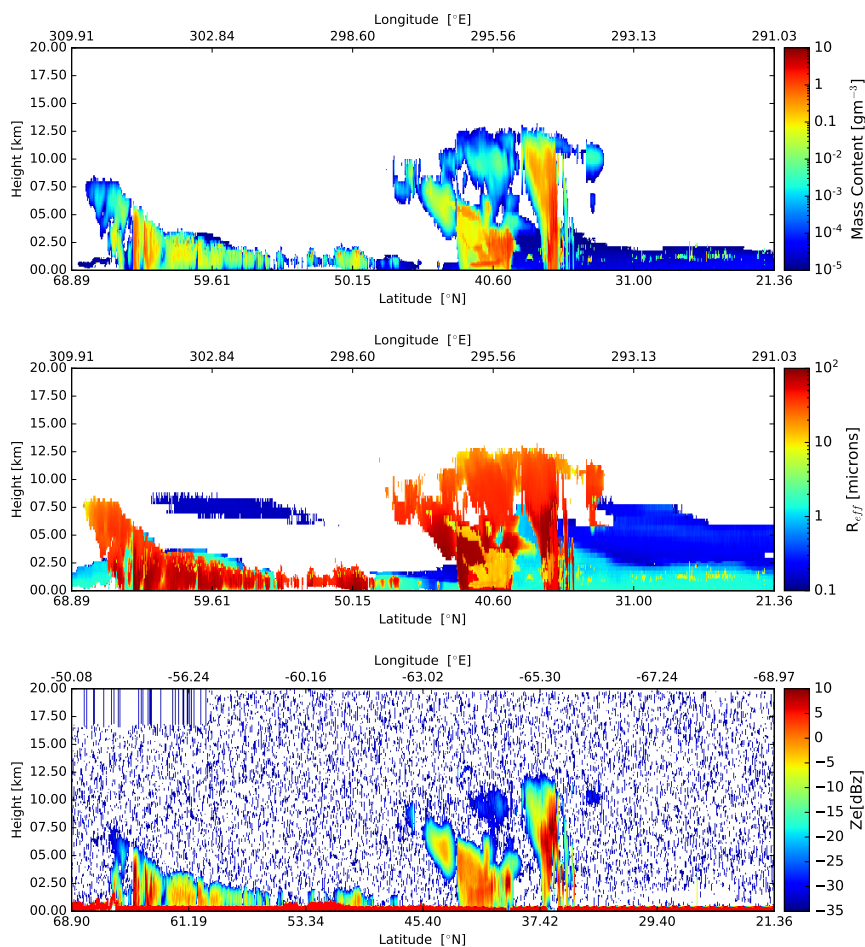
Figure 12. Cross-sections of the particle mass density, effective particle radius, and simulated observed Radar reflectivity, following the simulated EarthCARE orbit for the Halifax scene
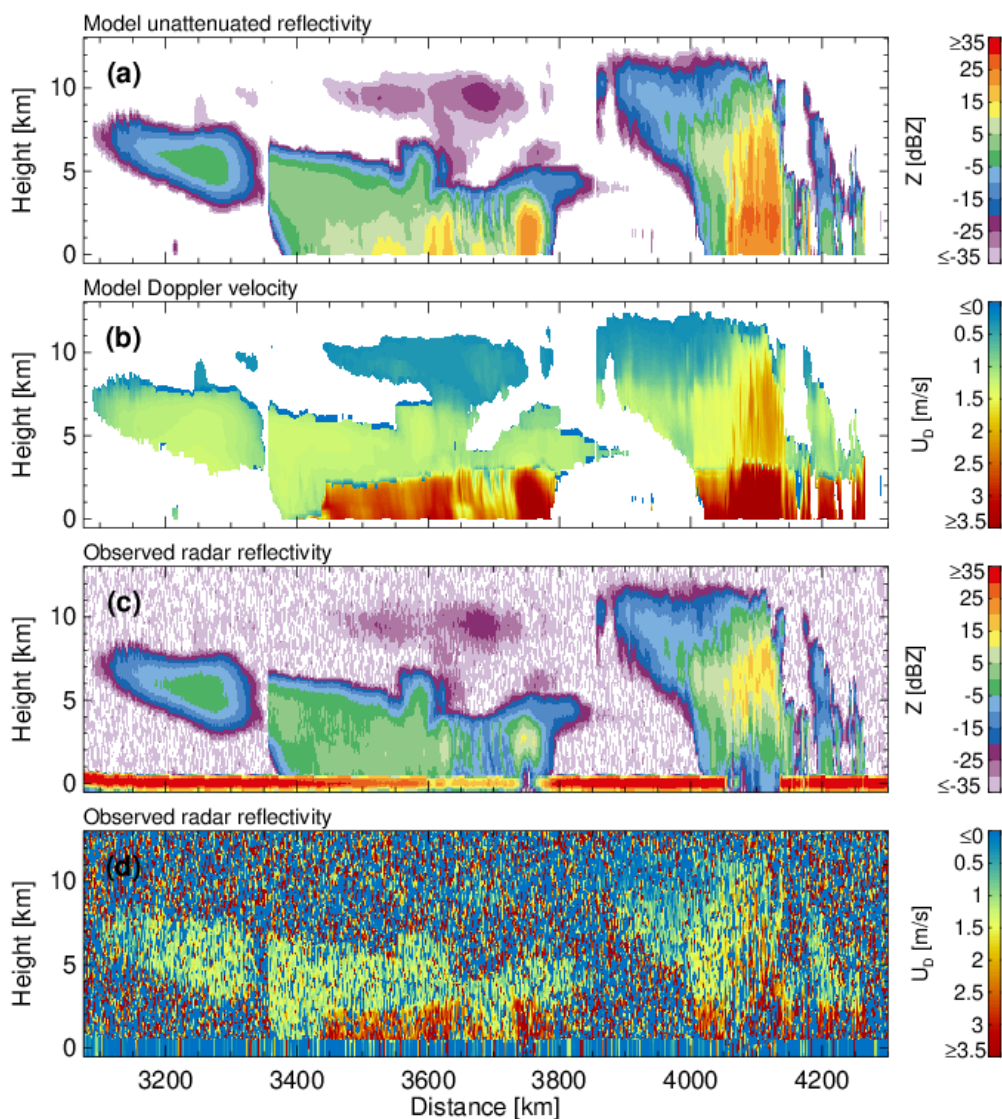
Figure 13. (a) GEM unattenuated 94-GHz radar reflectivity factor at the model resolution, (b) GEM sedimentation Doppler velocity at the model resolution, (c) CPR raw radar reflectivity factor at the CPR resolution with surface echo and (d) CPR raw Doppler velocity measurements with no correction applied at the CPR resolution with surface echo
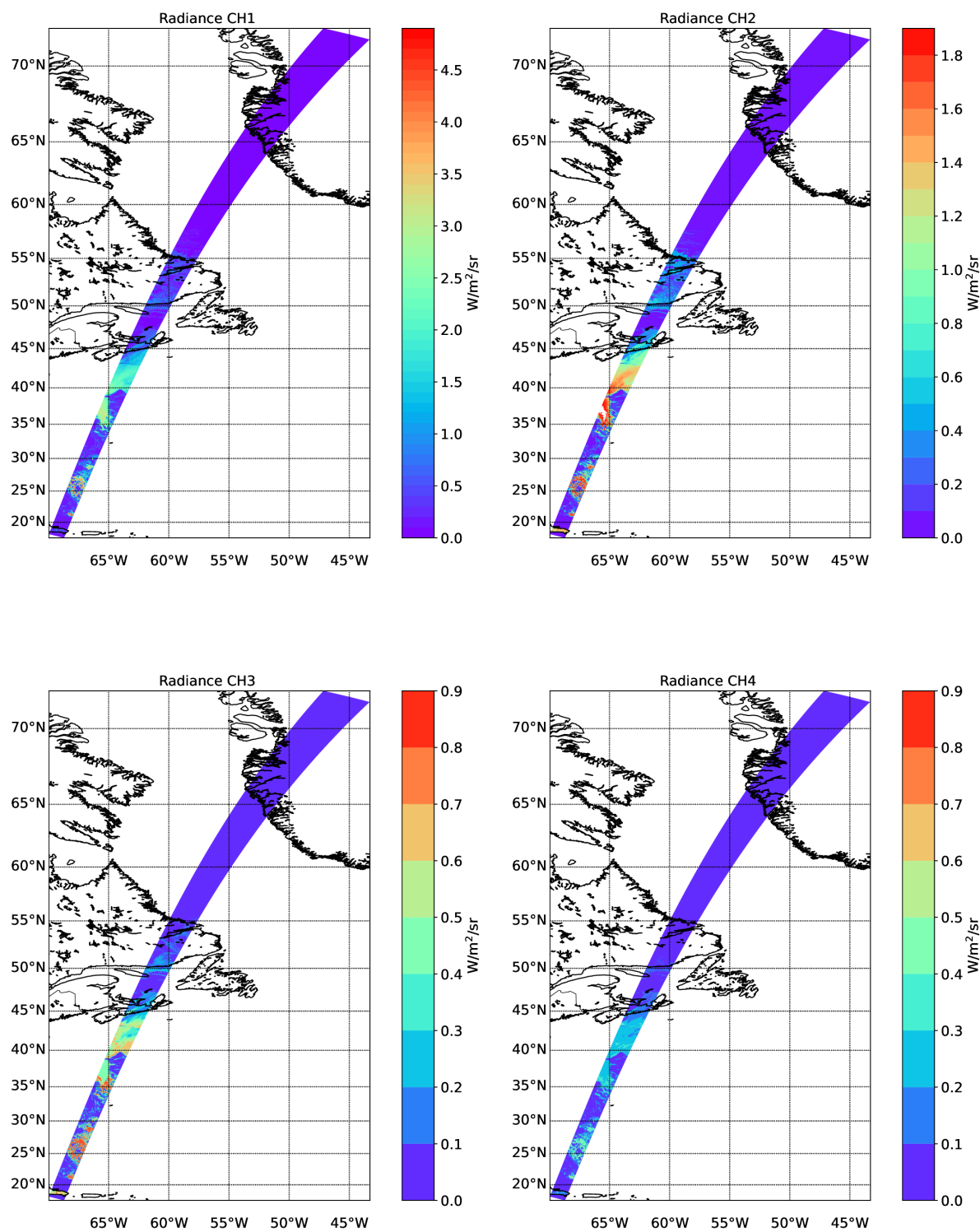
Figure 14. Simulated TOA radiances for the 4 SW EarthCARE MSI channels for the Halifax scene.
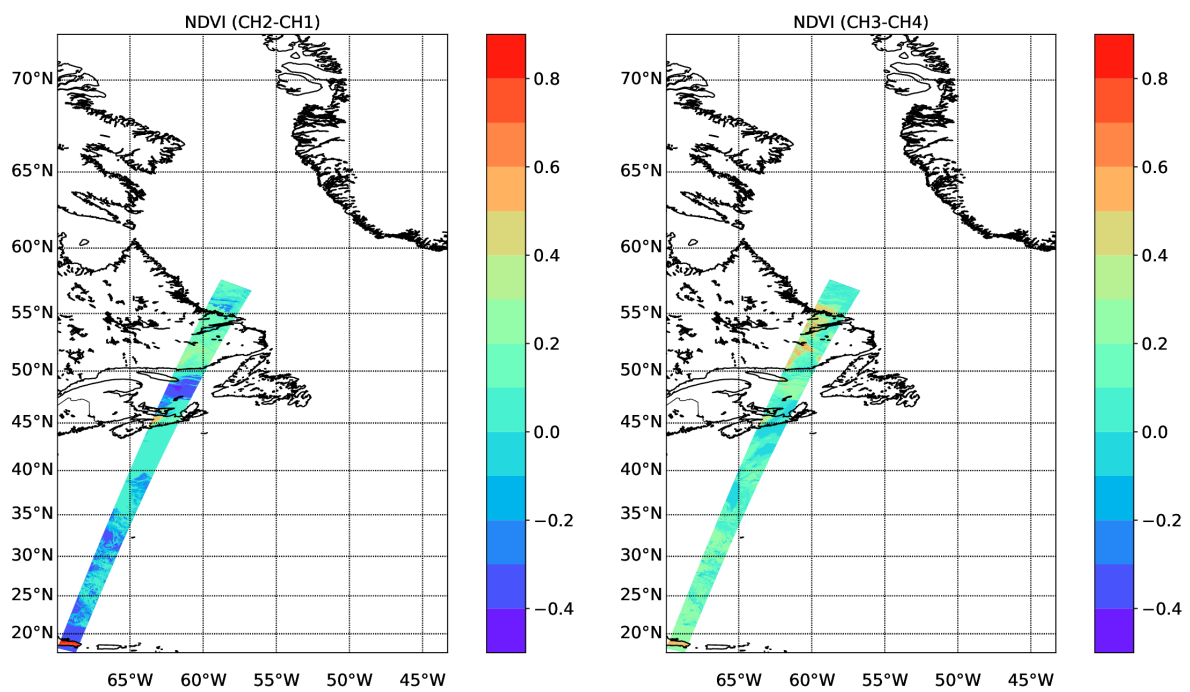
Figure 15. NDVI values corresponding to the simulated radiances shown in Fig. 14
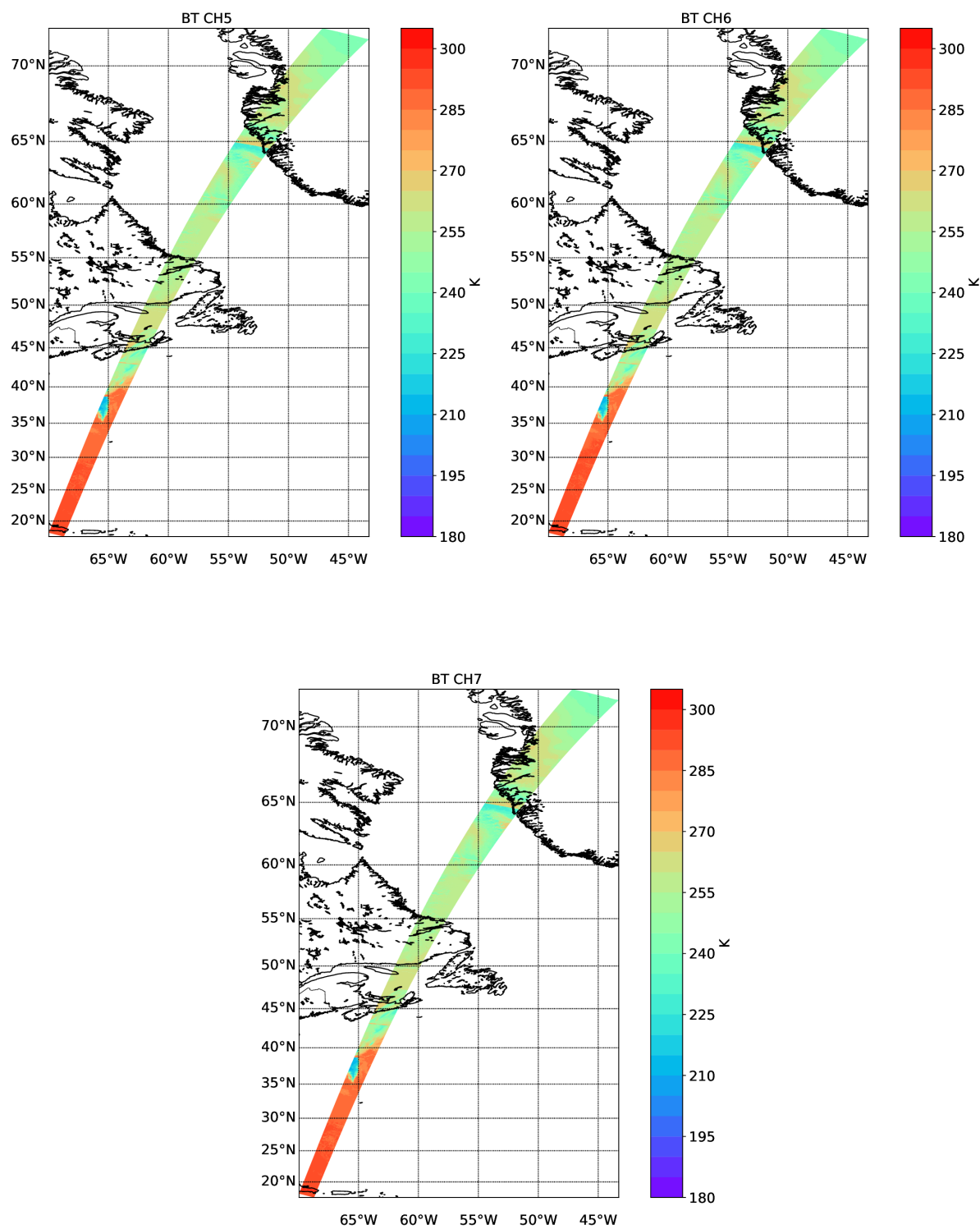
Figure 16. Simulated TOA brightness-temperatures for the three LW EarthCARE MSI channels for the Halifax scene.
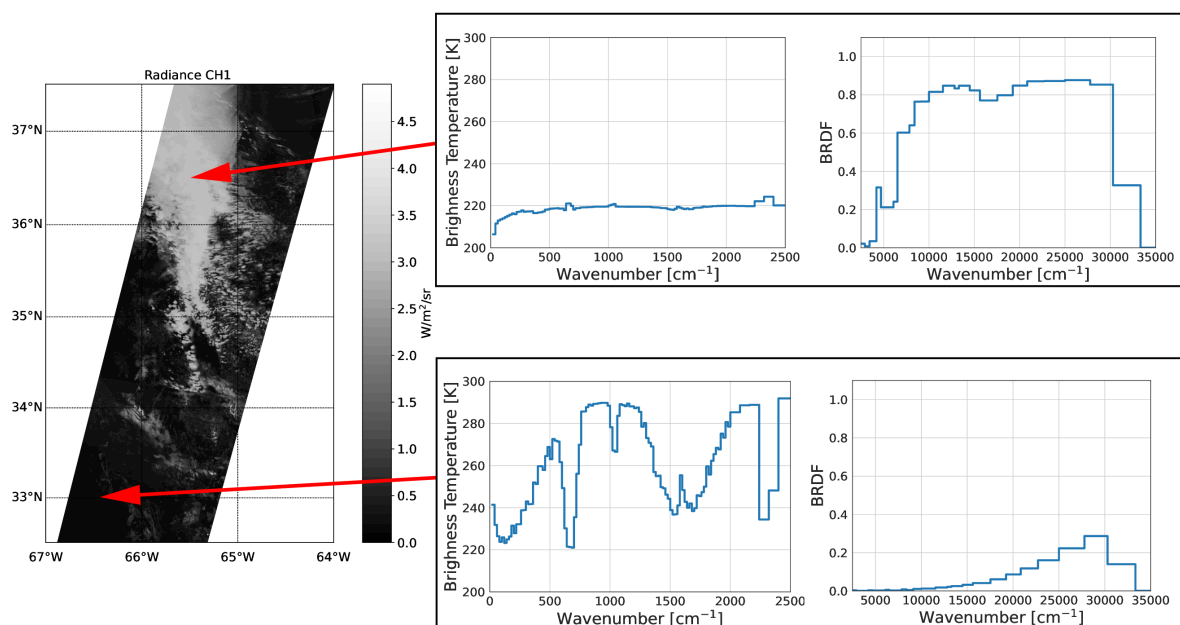
Figure 17. Left Panel: TOA channel 1 radiances for the Halifax scene between 32.5°N and 37.5°N. Right-Top: LW brightness temperatures and SW BRDFs as a function of wavenumber corresponding to a high altitude thick cloud. Right-Bottom: LW brightness temperatures and SW BRDFs for each BBR channel corresponding to cloud-free conditions over ocean.

3.2 Baja

The Baja scene is the 2nd GEM derived scene. This scene has a lot of topographical variation compared to the Halifax scene

470 and contains large regions of thinly distributed aerosols. In addition, high level ice clouds are present South of $35°N$. Near the center of the scene, above the Rocky mountains, extended regions of optically thick ice and water clouds are present.

The extinction, lidar-radio and depolarization model-truth fields for the nadir track are shown in Fig. 18. The lidar observed attenuated backscatter fields are shown in Fig. 19 while the particle mass-density, effective radius, equivalent radar reflectivity are shown in Fig. 20.
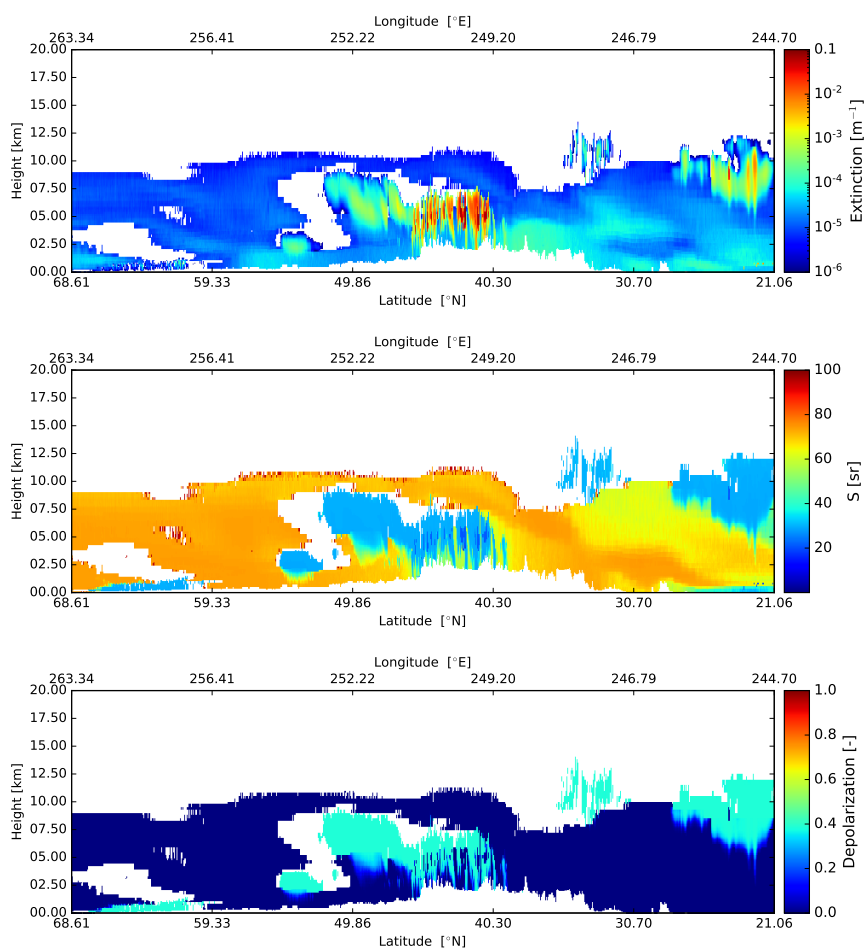
Figure 18. Cross-sections of the extinction at 355 nm, lidar extinction-to-backscatter ratio, and linear depolarization ratio, following the simulated EarthCARE orbit for the Baja scene

475 The GEM model and CPR simulated signals for selected region of the Baja scene are shown in 21. Due to the large horizontal extend of the scene, we focus on the $[45°; 55°N]$ simulated region that covers the northern part of the GEM simulation over the

33
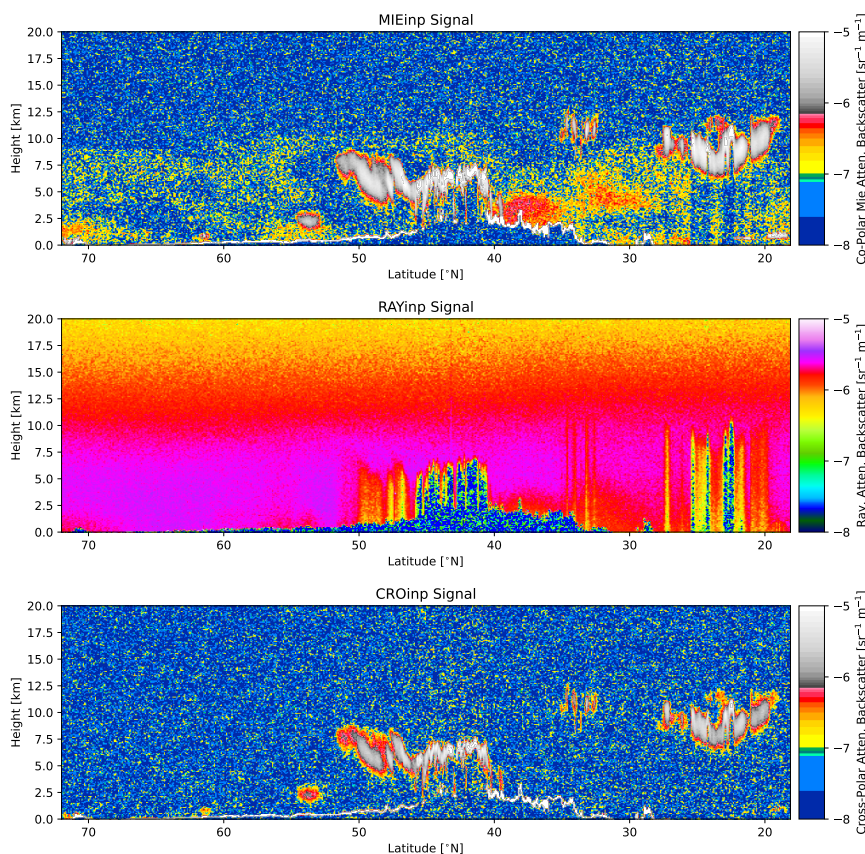
Figure 19. Simulated Mie channel, Rayleigh channel, and Cross-Polar ATLID attenuated backscatters for the Baja scene.

Rockies which includes ice clouds. The top two panels shows the unattenuated 94-GHz radar reflectivity and the reflectivity weighted hydrometeor sedimentation velocity at the GEM grid resolution. The ice clouds are characterized by low radar reflectivity and Doppler velocities that increase towards the hydrometeor layer base. Due to their low radar reflectivity, a significant fraction of the EarthCARE CPR echoes are close to its detection limit (-35 dBZ). The low radar reflectivities contribute to the noisiness of the CPR raw Doppler velocities.

The simulated short-wave TOA radiances for the MSI short-wave channels are shown in 22. Here north of about $55°$N snow and ice surfaces are present leading to high channel 1 and 2 radiances even when clear-sky is present. The snow-ice surfaces also stand out in the CH3-CH4 NDVI images (Fig. 23.

The simulated long-wave TOA brightness temperatures for the MSI long-wave channels are shown in Fig. 24. Here there are cold (but low altitude) clouds tops and surfaces north of $55°$ N visible, as are the cold (but high) cloud top temperatures around $45°$N. The warm land and ocean temperatures are also apparent in the mainly cloud-free region south of about $40°$ N.
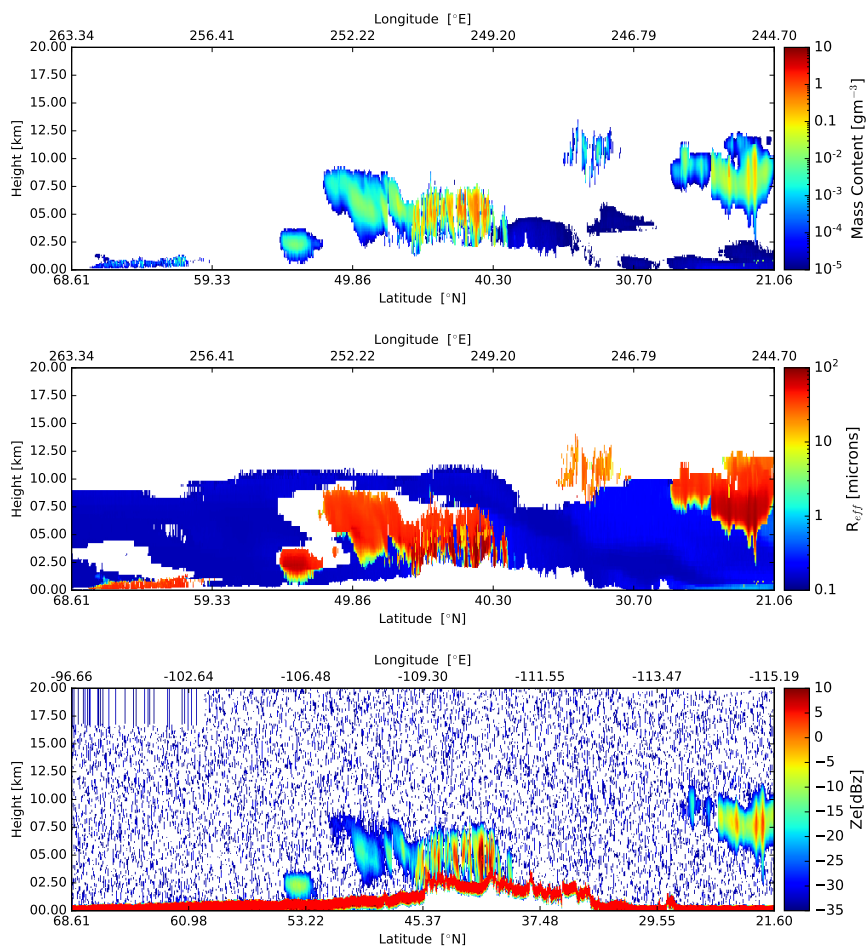
Figure 20. Cross-sections of the particle mass density, and effective particle radius, and observed Radar reflectivity, following the simulated EarthCARE orbit for the Baja scene.
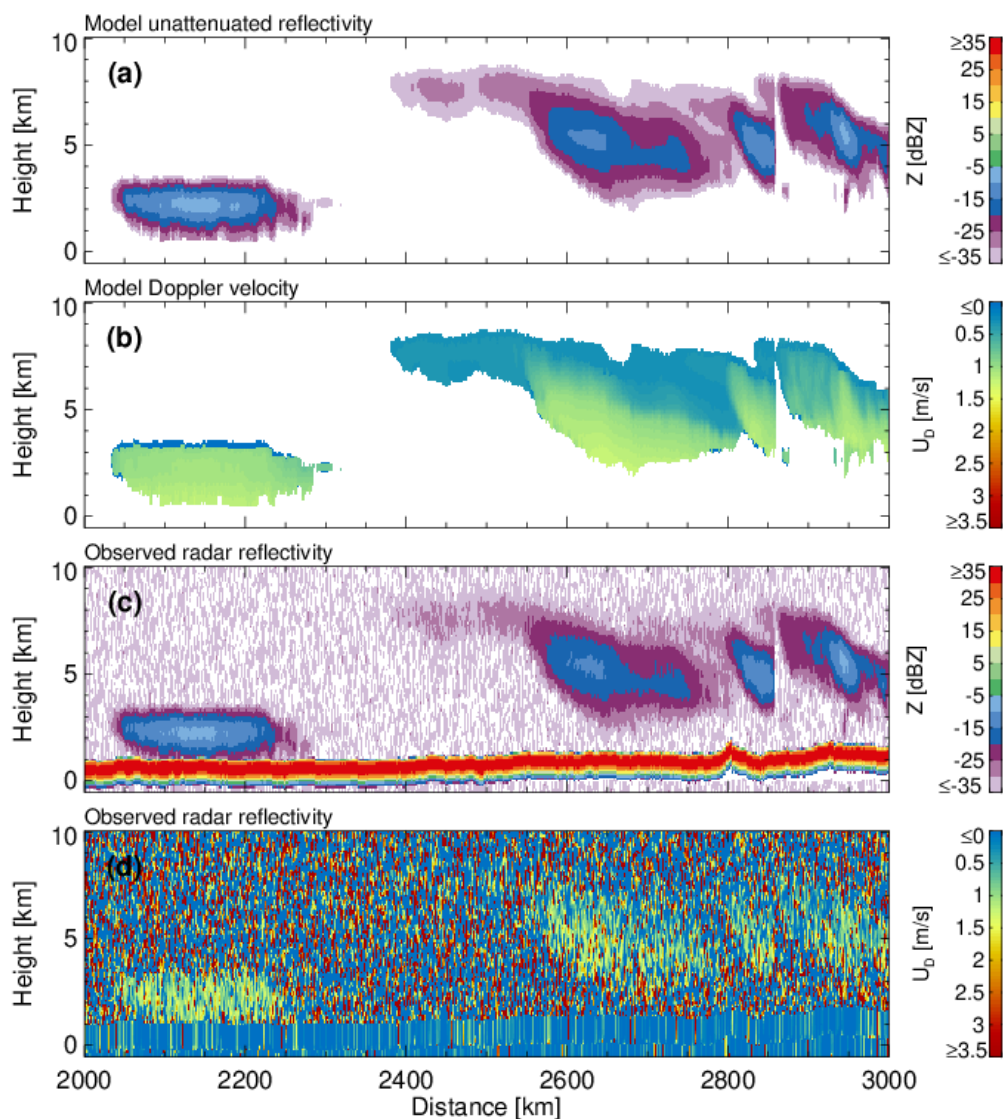
Figure 21. (a) GEM unattenuated 94-GHz radar reflectivity factor at the model resolution, (b) GEM sedimentation Doppler velocity at the model resolution, (c) CPR raw radar reflectivity factor at the CPR resolution with surface echo and (d) CPR raw Doppler velocity measurements with no correction applied at the CPR resolution with surface echo

Figure 22. Simulated TOA radiances for the 4 SW EarthCARE MSI channels for the Baja scene.
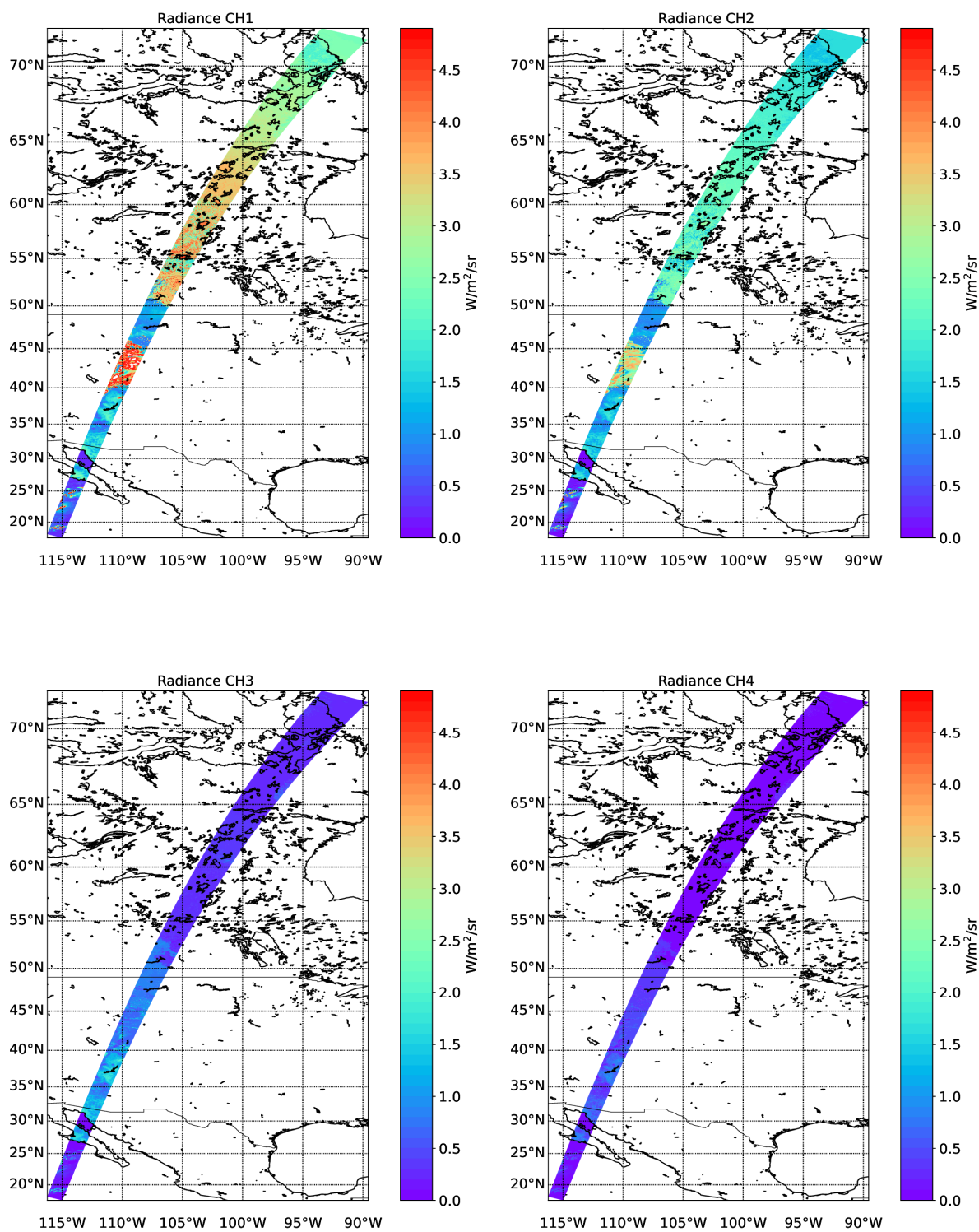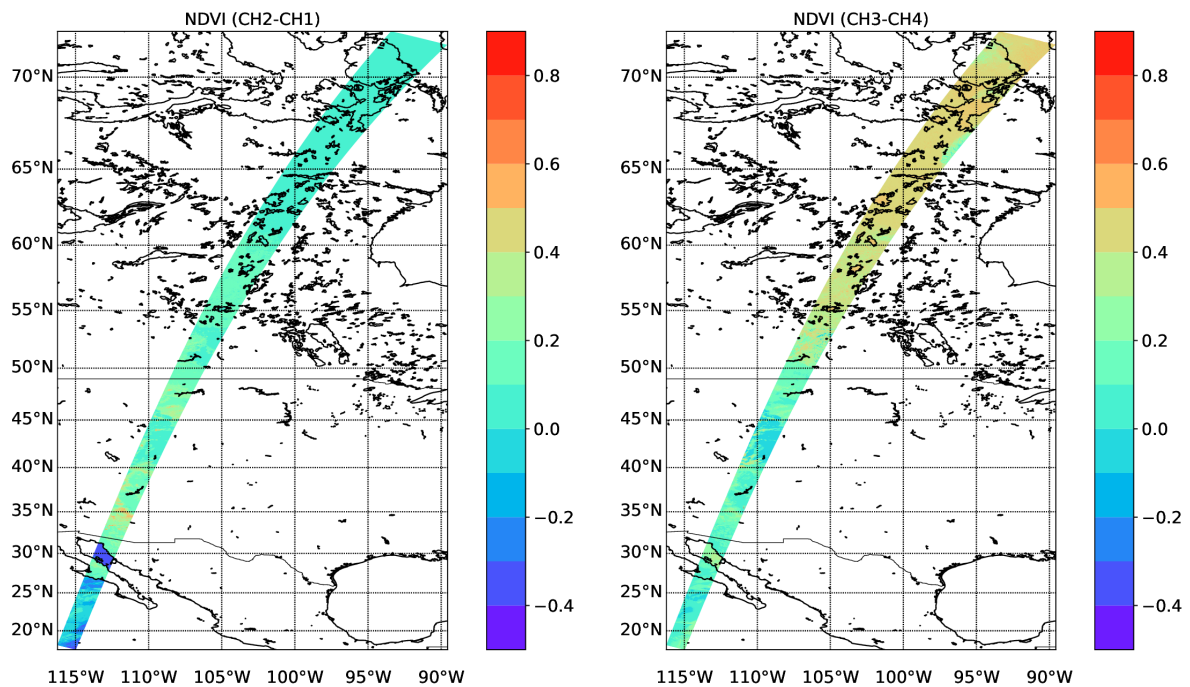
Figure 23. NDVI values corresponding to the simulated radiances shown in Fig. 22
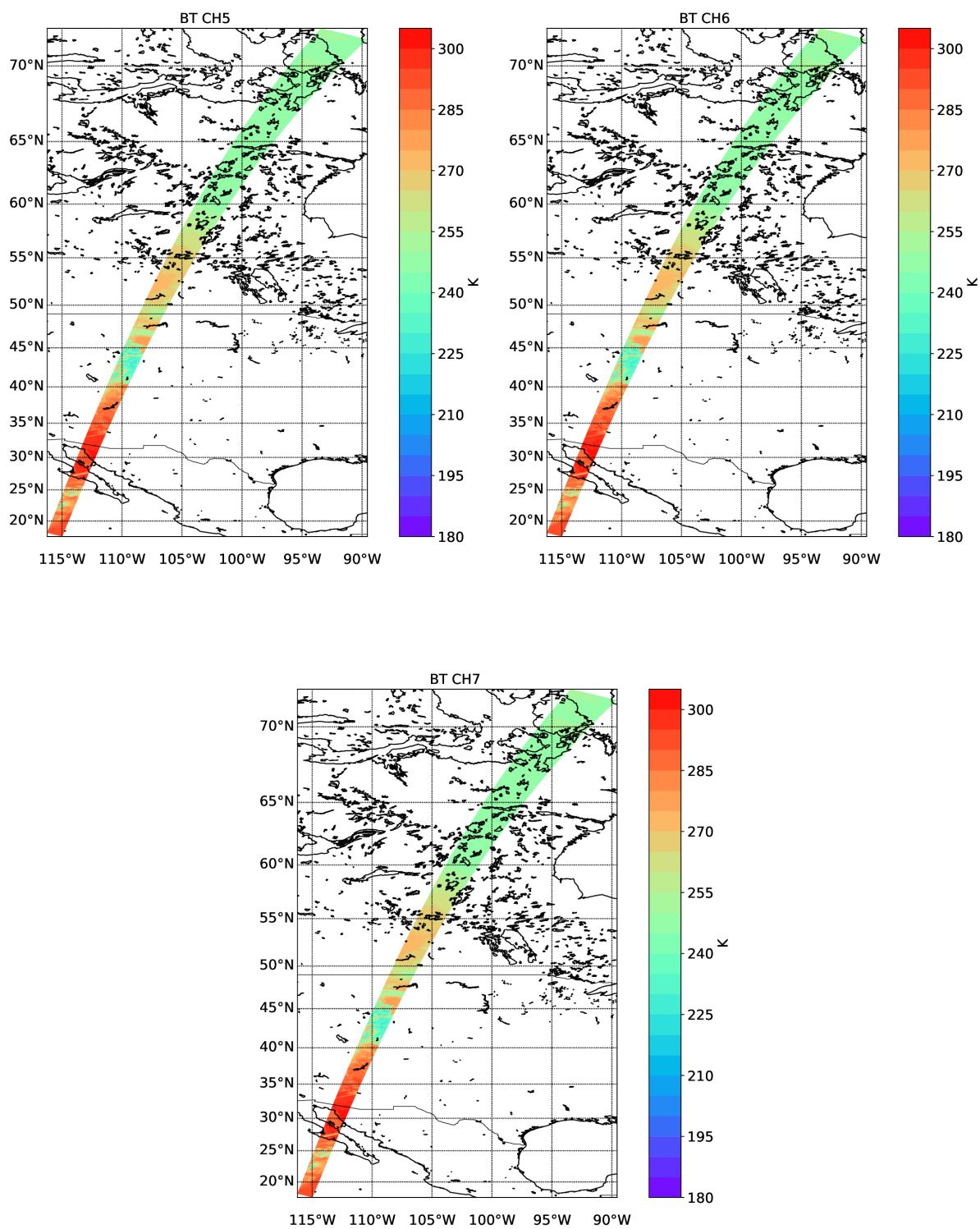
Figure 24. Simulated TOA brightness-temperatures for the 3 LW EarthCARE MSI channels for the Baja scene.

3.3 Hawaii

The 3rd GEM based scene is the Hawaii scene, situated almost completely over ocean, where the nadir track is completely over
490 ocean while a few of the smaller Hawaiian islands are within the MSI track. This scene exhibits areas of clear-sky, upper level
cirrus and a tropical convective system near the center of the scene. The extinction, lidar-ratio and depolarization model-truth
fields for the nadir track are shown in Fig. 25. The lidar observed attenuated backscatter fields are shown in Fig. 26 while the
particle mass-density, effective radius, equivalent radar reflectivity are shown in Fig. 27.
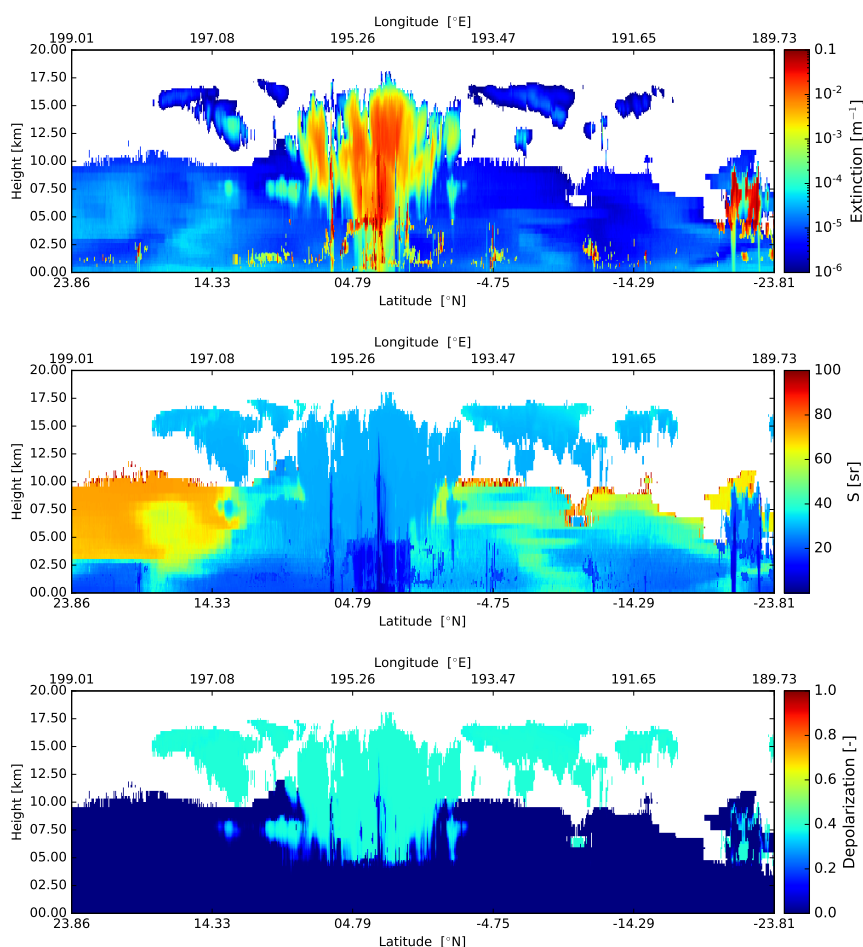
Figure 25. Cross-sections of the extinction at 355 nm, lidar extinction-to-backscatter ratio, and linear depolarization ratio, following the
simulated EarthCARE orbit for the Hawaii scene

The GEM model and CPR simulated signals for the Hawaii scene are shown in Fig. 28. Due to the large horizontal extend of
495 the scene, we focus on the center of the scene where a large tropical convective/stratiform precipitating system was simulated.
The top two panels shows the unattenuated 94-GHz radar reflectivity and the reflectivity weighted hydrometeor sedimentation

40
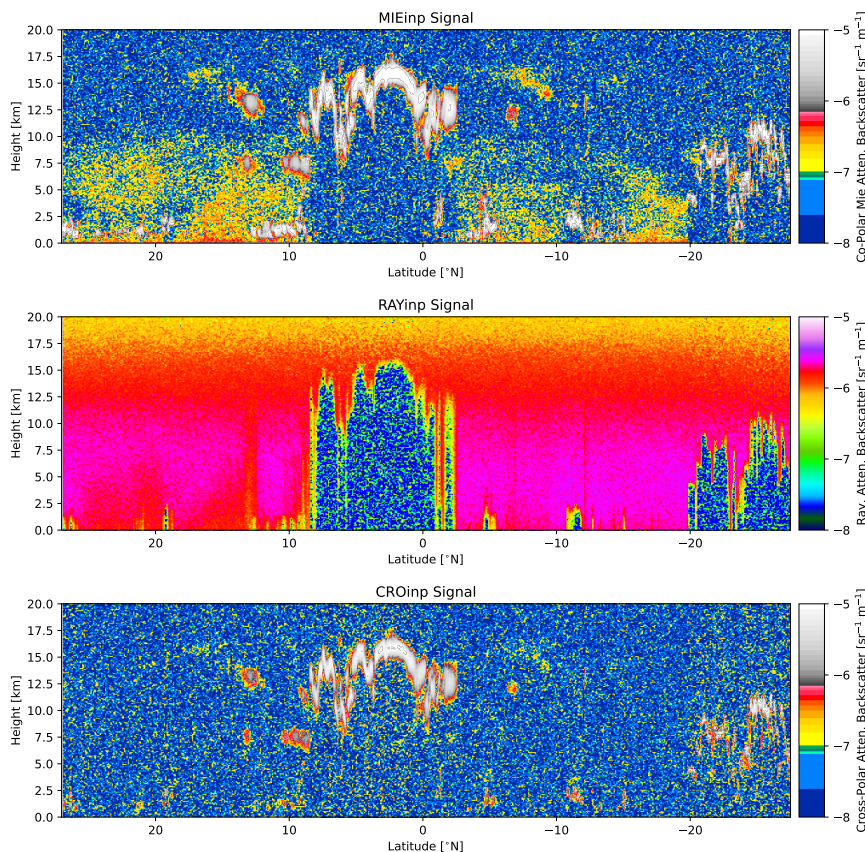
Figure 26. Simulated Mie channel, Rayleigh channel, and Cross-Polar ATLID attenuated backscatters for the Hawaii scene.

velocity at the GEM grid resolution. The widespread stratiform precipitation is extensive covering over 500 km and the precipitation system reaches tops of $16km$. Embedded convective cells are simulated at 2375 and 2750 km along track distance. The lower two panels show the raw (uncorrected) CPR radar reflectivity and mean Doppler velocity measurements. The Earth-CARE CPR has sufficient sensitivity to detect the hydrometeor layers except for weak reflectivity echoes near the highest cloud tops. The strong 94-GHz attenuation by hydrometeors results to significant attenuation in the rain layer and complete loss of the surface echo return in the two embedded convective cells. Significant multiple scattering is simulated at 2750 km, as seen by the fainted CPR echoes that fill the surface echo gap around 4100 km due to multiple scattering (Battaglia et al., 2010). As expected, the CPR raw Doppler velocity field (500 m along track integration) is noisy (Kollias et al., 2014, 2022a). Despite their noisiness, the CPR Doppler velocities reproduce the main features of the GEM model Doppler velocities, namely, the transition from solid to liquid hydrometeors and the low sedimentation Doppler velocities in the upper cloud levels.

The simulated short-wave TOA radiances for the MSI short-wave channels are shown in Fig. 29. Here the cloud features are all clearly visible against the low albedo ocean. The NDVI fields are shown in Fig. 30. The high-values in the right-panel correspond to one of the few land-areas (the island of Niihau) within the MSI swath.
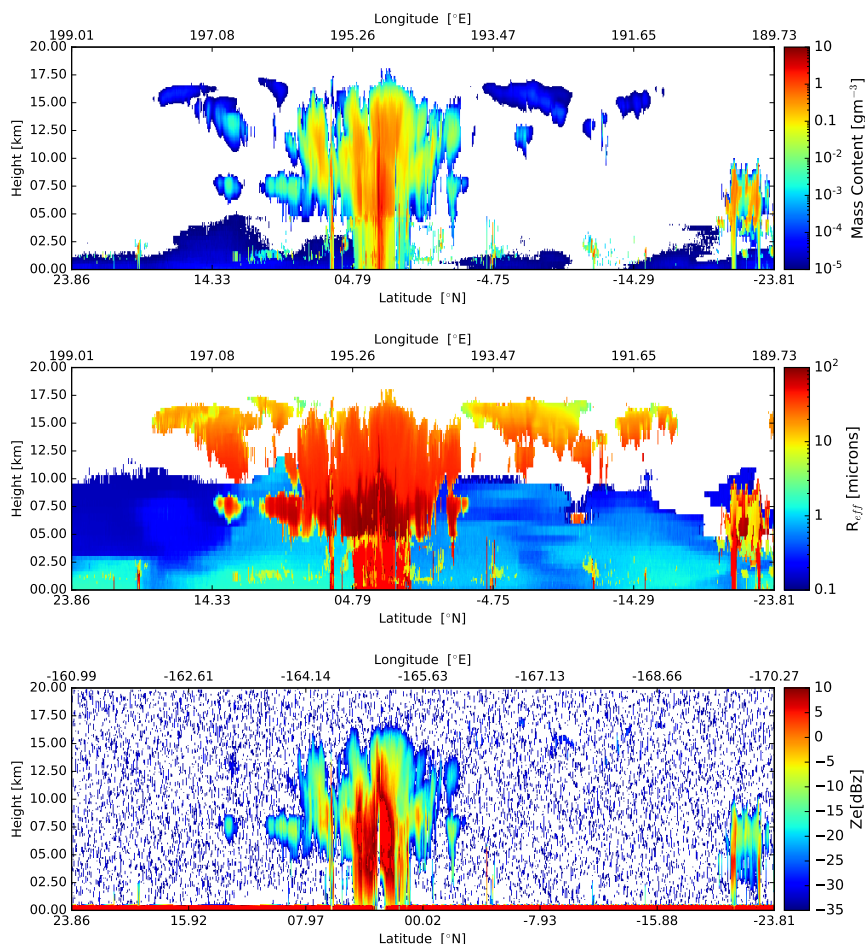
Figure 27. Cross-sections of the particle mass density, and effective particle radius, and observed Radar reflectivity, following the simulated EarthCARE orbit for the Hawaii scene

510   The simulated long-wave TOA brightness temperatures for the MSI long-wave channels are shown in Fig. 31. Here the very cold cloud tops near the center of the scene are especially prominent.

3.4   Halifax Aerosol Scene

As a last test scene based on GEM and CAMS inputs and used in the processor development within this special issue, a mainly aerosol scene was built from a sub-section of the Halifax scene. For this "Halifax-aerosol" scene the region south of 36°N was
515   used, however, all liquid clouds and aerosol types were removed except for the coarse-mode non-absorbing aerosol (Sea-Salt). The remaining aerosol particle density was scaled by a factor of 2 to increase the total optical thickness and detectability by the MSI instrument. The resulting scene contains ice cloud north of about 33 °N and an aerosol rich boundary-layer marine
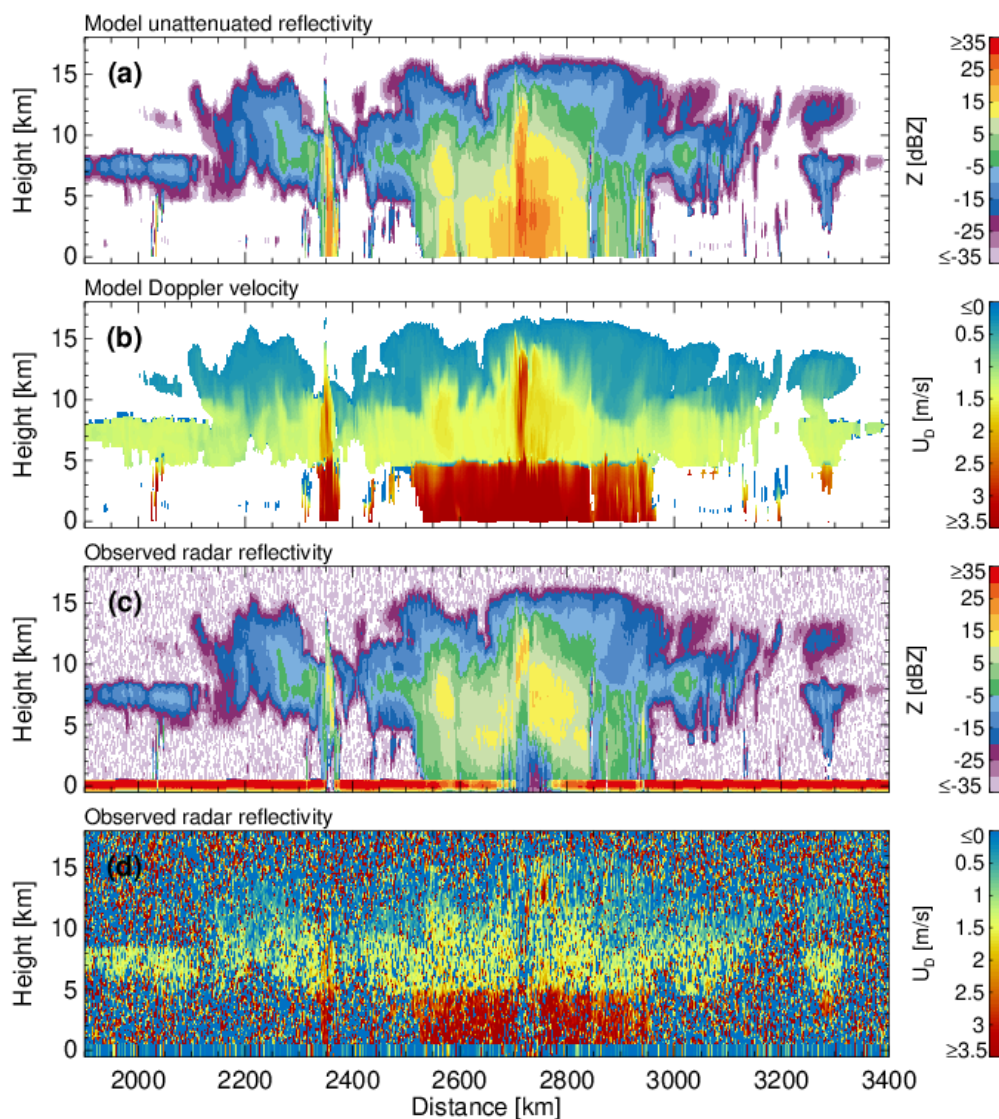
Figure 28. (a) GEM unattenuated 94-GHz radar reflectivity factor at the model resolution, (b) GEM sedimentation Doppler velocity at the model resolution, (c) CPR raw radar reflectivity factor at the CPR resolution with surface echo and (d) CPR raw Doppler velocity measurements with no correction applied at the CPR resolution with surface echo.

aerosol layer limited to an altitude of about 2.5km with a very tenuous layer above. The lidar observed attenuated backscatter fields are shown in Fig. 32, while the MSI images are shown in Figs. 33–35.
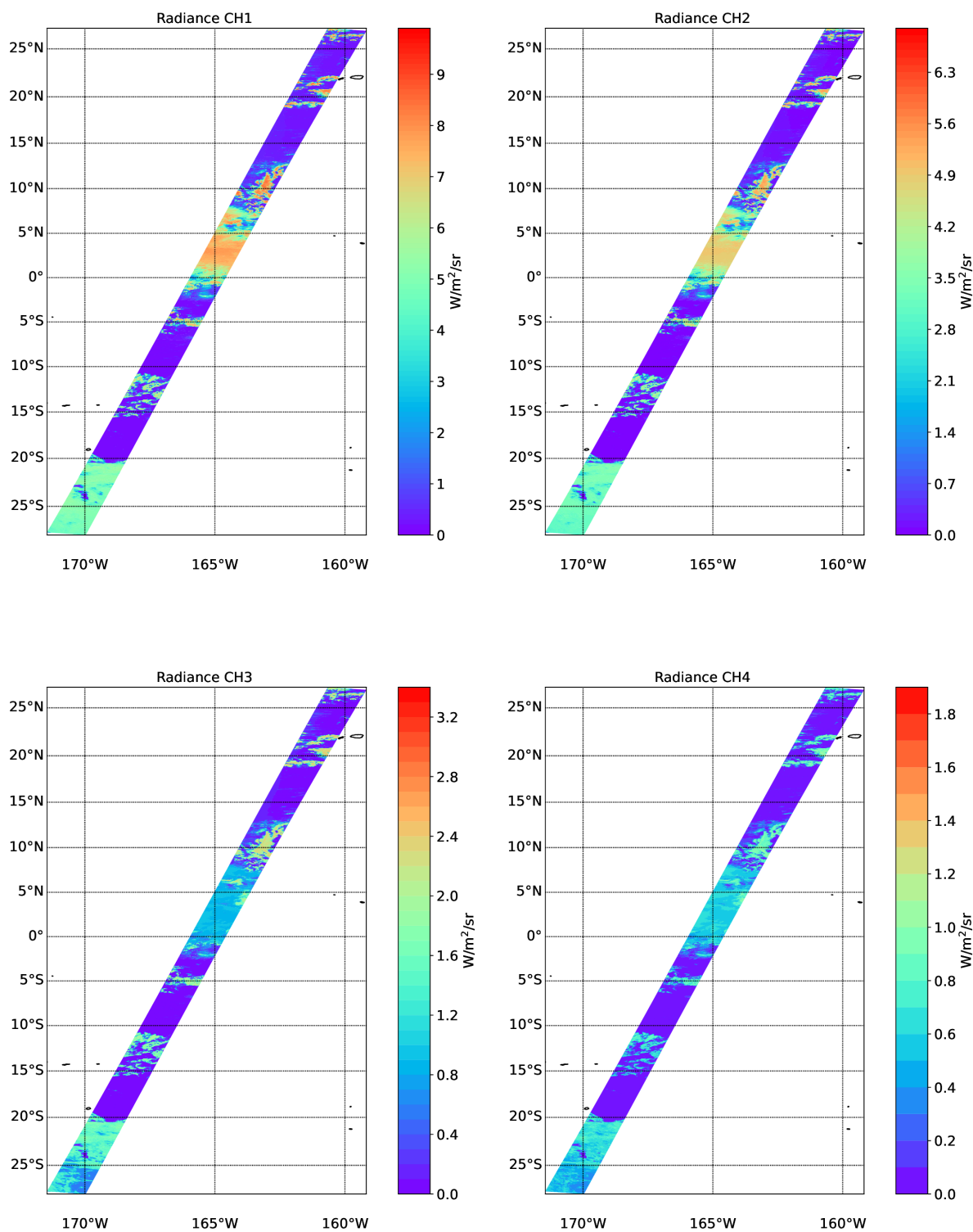
Figure 29. Simulated TOA radiances for the 4 SW EarthCARE MSI channels for the Hawaii scene.
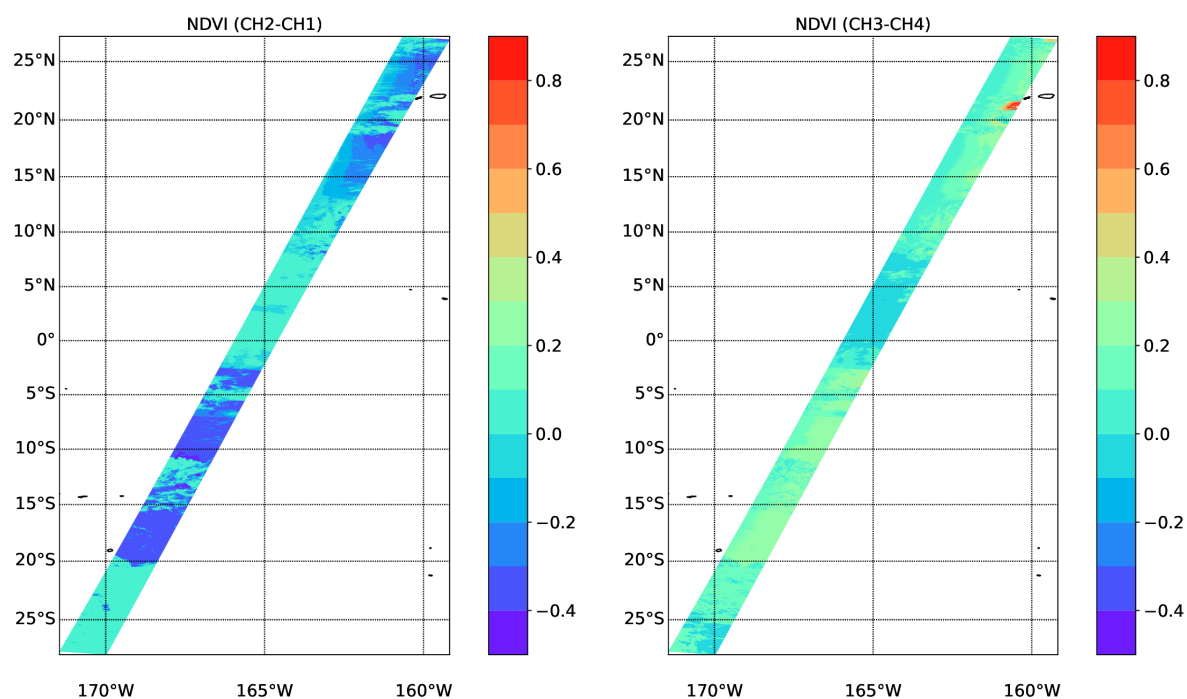
Figure 30. NDVI values corresponding to the simulated radiances shown in Fig. 29
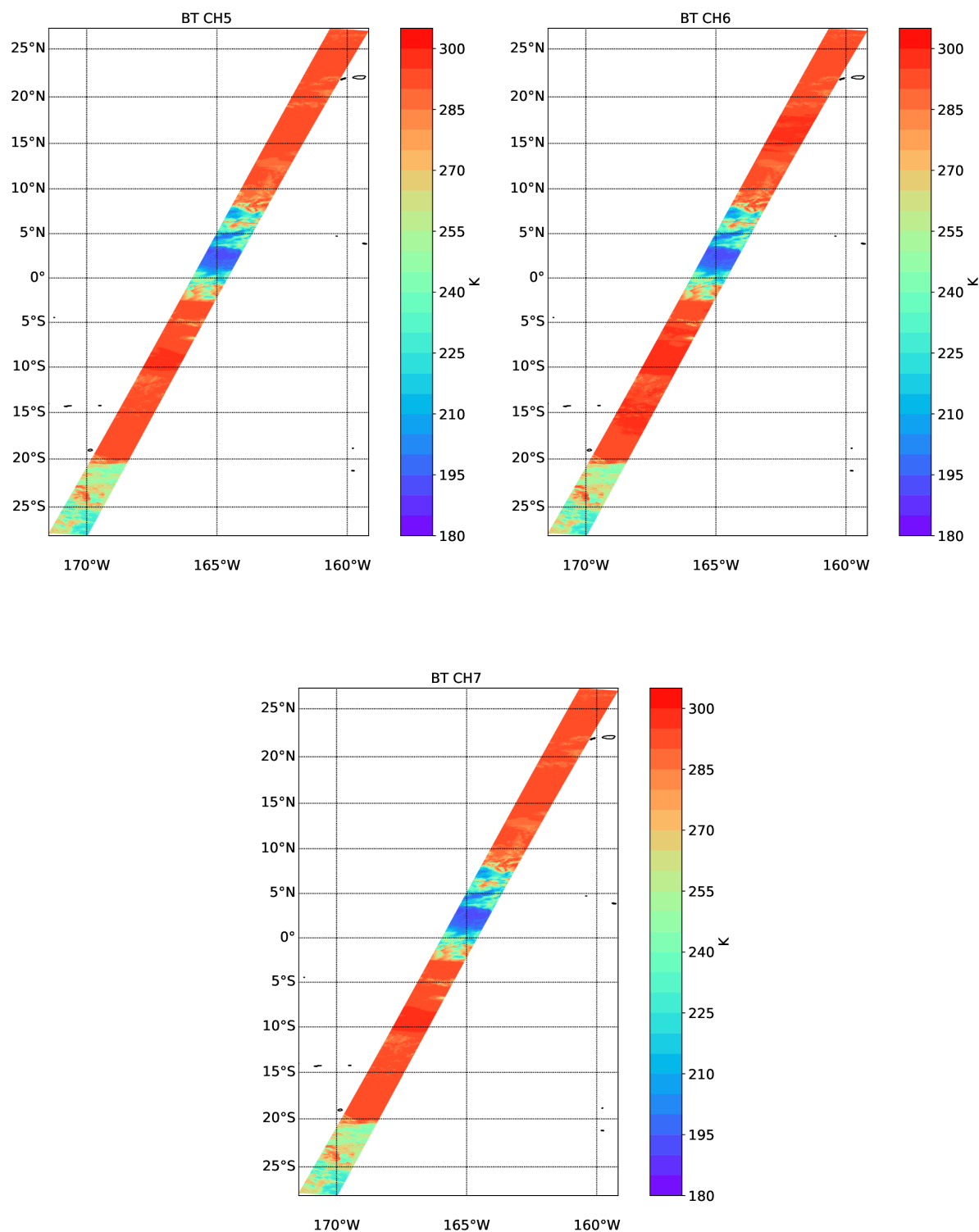
Figure 31. Simulated TOA brightness-temperatures for the 3 LW EarthCARE MSI channels for the Hawaii scene.
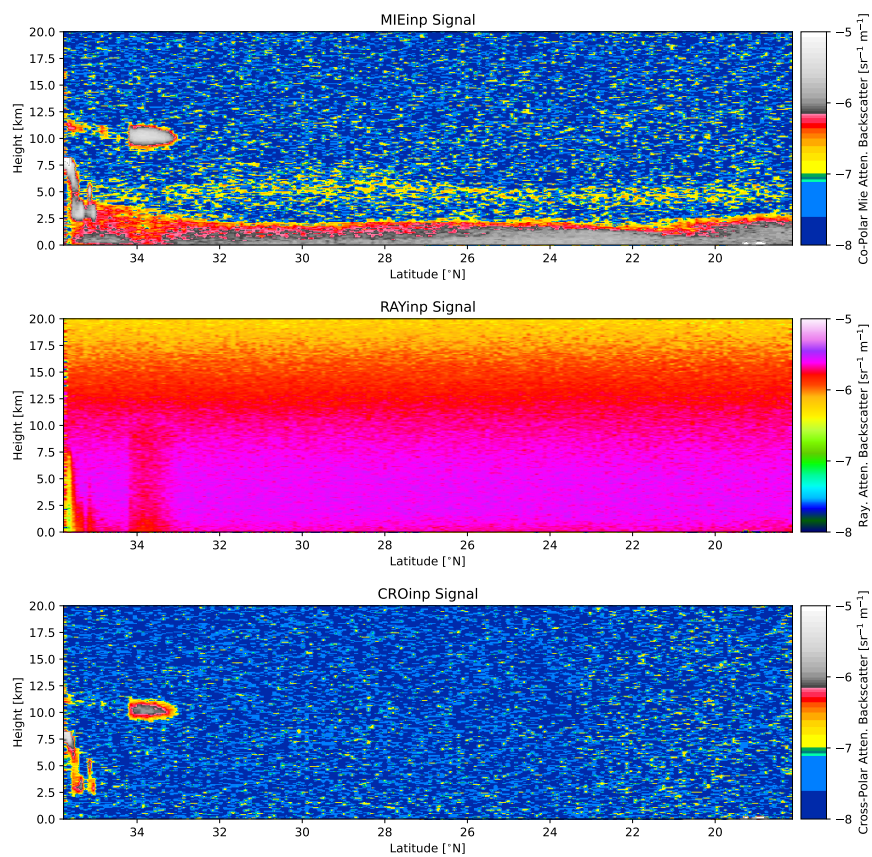
Figure 32. Simulated Mie channel, Rayleigh channel, and Cross-Polar ATLID attenuated backscatters for the Halifax-Aerosol scene.
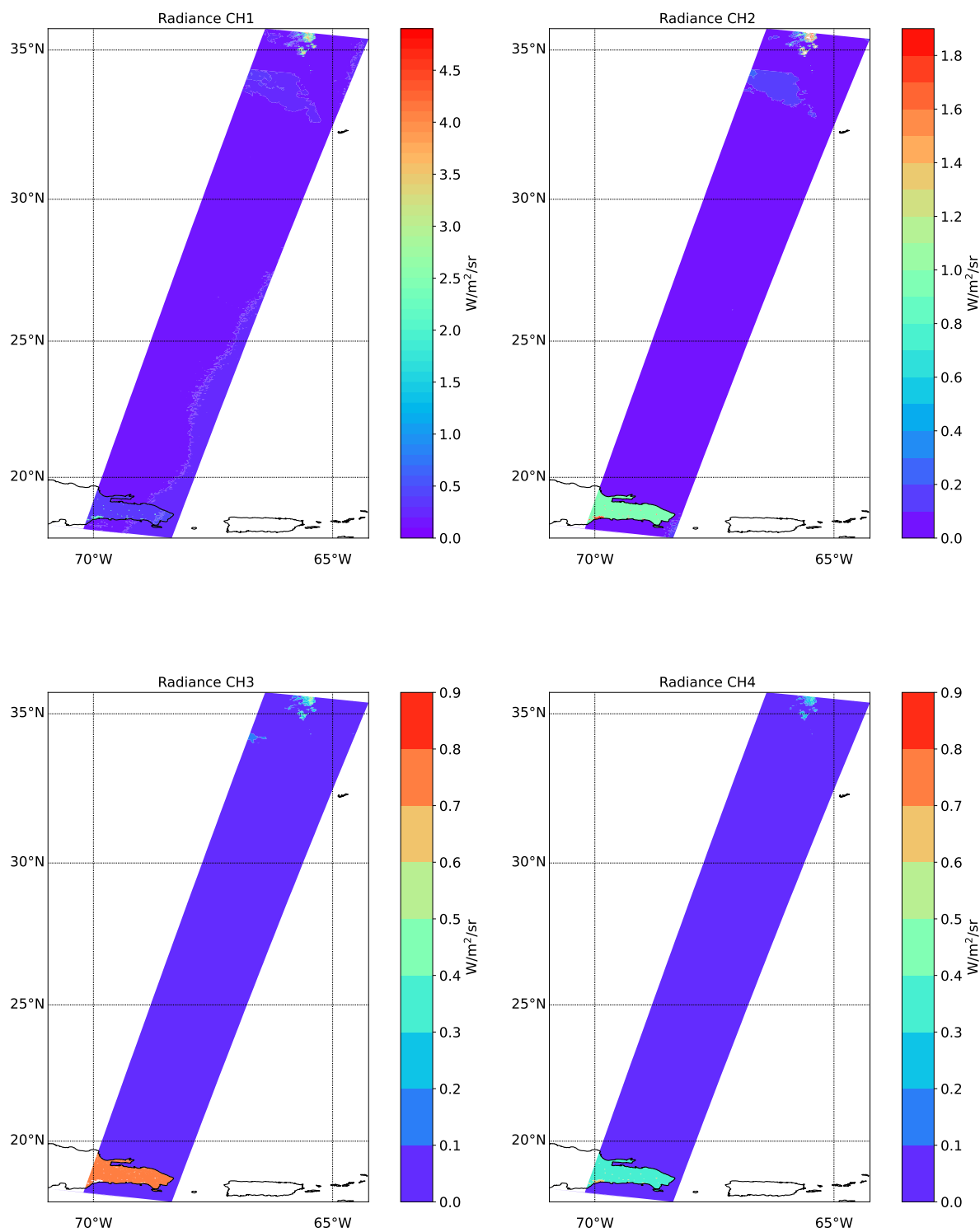
**Figure 33.** Simulated TOA radiances for the 4 SW EarthCARE MSI channels for the Halifax-Aerosol scene.
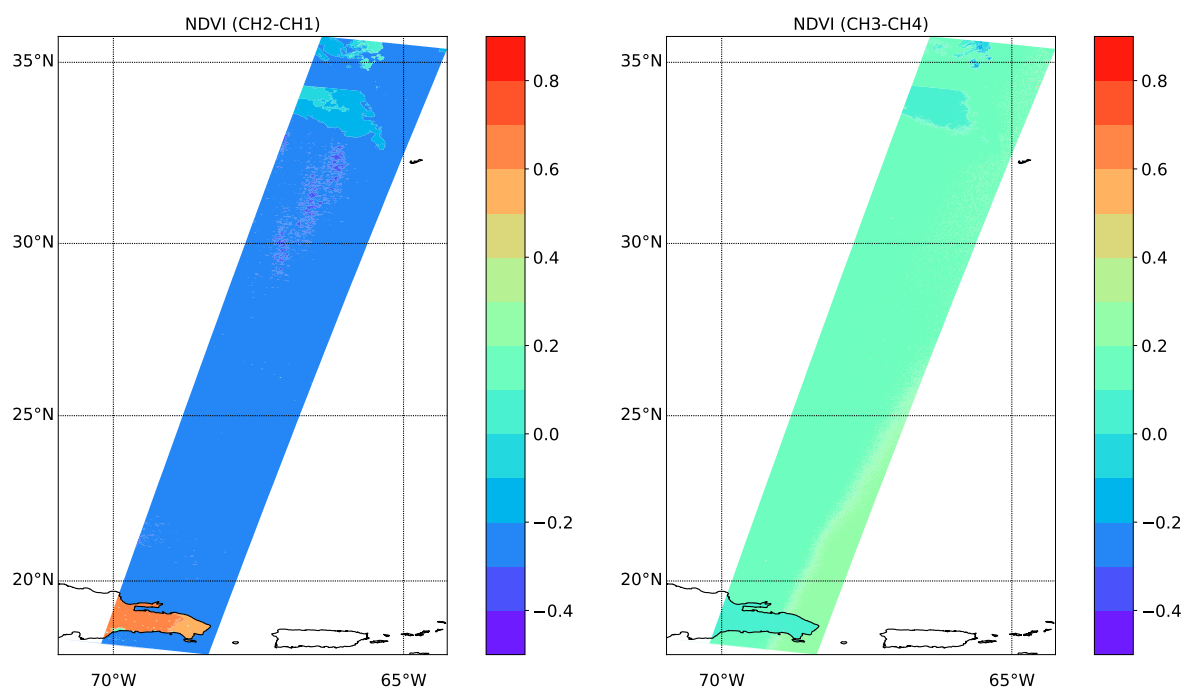
Figure 34. NDVI values corresponding to the simulated radiances shown in Fig. 33
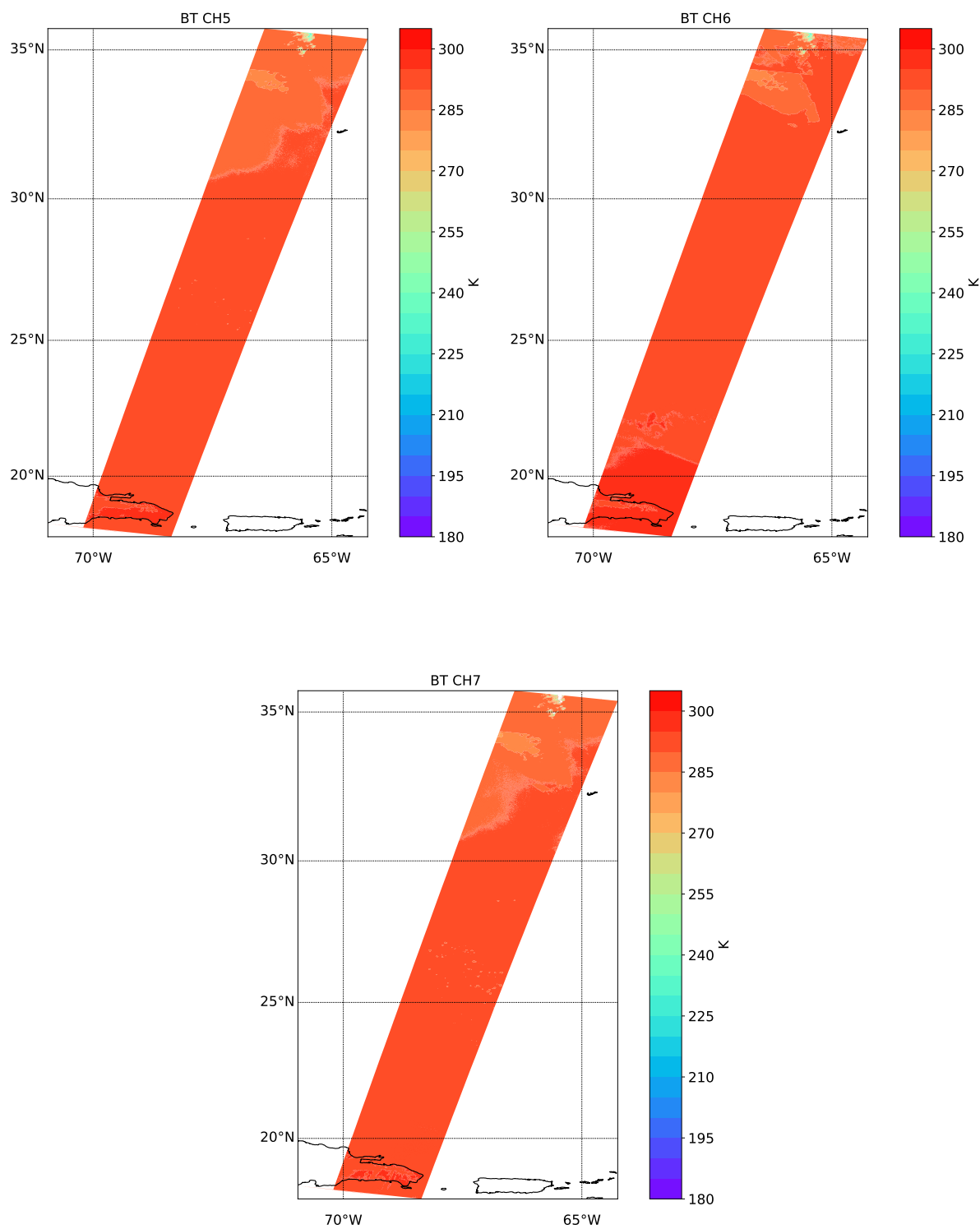
Figure 35. Simulated TOA brightness-temperatures for the 3 LW EarthCARE MSI channels for the Hawaii scene.

4 Conclusion

The detail, realism, physical consistency and scale of the tests scenes developed for EarthCARE algorithm development, implementation, and testing comprise a unique effort. The creation of detailed realistic test scenes has involved considerable work but should be judged as time well spent. Not only have they served to develop new scientific inversion approaches, but have also proved very useful in terms of technical development. It is true that the success of any inversion procedure must be evaluated using real data, however, the ability to compare against a "model truth" is invaluable when constructing new inversion algorithms, both in a scientific sense and in a technical (e.g. debugging) sense.

When actual EarthCARE data is available, there will, no doubt, be surprises to be dealt with. The extensive algorithm development process, aided by the simulations, will help ensure that these unexpected issues will be handled efficiently.

Competing interests. The authors declare that they have no conflict of interest.

References

Barker, H. and Li, J.: Accelerating Radiative Transfer Calculations for High-Resolution Atmospheric Models, Quarterly Journal of the Royal
540   Meteorological Society, 145, https://doi.org/10.1002/qj.3543, 2019.

Barker, H. W., Cole, J. N. S., Qu, Z., Villefranque, N., and Shephard, M.: EarthCARE's Continuous Radiative Closure Assessment: Summary
and Application to Data from a Synthetic Observing System, Atmospheric Measurement Techniques, to be submitted, 2022.

Battaglia, A., Tanelli, S., Kobayashi, S., Zrnic, D., Hogan, R. J., and Simmer, C.: Multiple-scattering in radar systems: A review, Journal of
Quantitative Spectroscopy and Radiative Transfer, 111, 917–947, https://doi.org/10.1016/j.jqsrt.2009.11.024, 2010.

545 Baum, B. A., Yang, P., Heymsfield, A. J., Bansemer, A., Cole, B. H., Merrelli, A., Schmitt, C., and Wang, C.: Ice cloud single-scattering
property models with the full phase matrix at wavelengths from 0.2 to $100\mu m$, Journal of Quantitative Spectroscopy and Radiative Transfer,
146, 123–139, https://doi.org/https://doi.org/10.1016/j.jqsrt.2014.02.029, electromagnetic and Light Scattering by Nonspherical Particles
XIV, 2014.

Brandes E. A., Zhang, G. and J., V.: Developing and bounding ice particle mass- and area-dimension expressions for use in atmospheric
550   models and remote sensing, J. Appl. Meteor. Climatol., p. 674–685, https://doi.org/10.1175/1520-0450(2002)041, 2002.

Chang, M.: Overview of the EarthCARE multi-spectral imager and results from the development of the MSI engineering model, in: Inter-
national Conference on Space Optics — ICSO 2012, edited by Cugny, B., Armandillo, E., and Karafolas, N., vol. 10564, p. 105643Z,
International Society for Optics and Photonics, SPIE, https://doi.org/10.1117/12.2551545, 2019.

do Carmo, J. P., Hélière, A., Le Hors, L., Toulemont, Y., Lefebvre, A., and Lefebvre, A.: ATLID, ESA Atmospheric LIDAR Developement
555   Status, EPJ Web of Conferences, 119, 04 003, https://doi.org/10.1051/epjconf/201611904003, 2016.

do Carmo, J. P., de Villele, G., Wallace, K., Lefebvre, A., Ghose, K., Kanitz, T., Chassat, F., Corselle, B., Belhadj, T., and Bravetti, P.:
ATmospheric LIDar (ATLID): Pre-Launch Testing and Calibration of the European Space Agency Instrument That Will Measure Aerosols
and Thin Clouds in the Atmosphere, Atmosphere, 12, https://doi.org/10.3390/atmos12010076, 2021.

Donovan, D. P., Klein Baltink, H., Henzing, J. S., de Roode, S. R., and Siebesma, A. P.: A depolarisation lidar-based method for the
560   determination of liquid-cloud microphysical properties, Atmospheric Measurement Techniques, 8, 237–266, https://doi.org/10.5194/amt-
8-237-2015, 2015.

Eisinger, M., Wehr, T., Kubota, T., Bernaerts, D., and Wallace, K.: The EarthCARE production model and auxiliary products, Atmospheric
Measurement Techniques, to be submitted, 2022.

Erfani, E. and Mitchell, D. L.: Developing and bounding ice particle mass- and area-dimension expressions for use in atmospheric models
565   and remote sensing, Atmospheric Chemistry and Physics, p. 4379–4400, https://doi.org/10.5194/acp-16-4379-2016, 2016.

Fell, F. and Fischer, J.: Numerical simulation of the light field in the atmosphere–ocean system using the matrix-operator method, Journal of
Quantitative Spectroscopy and Radiative Transfer, 69, 351–388, https://doi.org/https://doi.org/10.1016/S0022-4073(00)00089-3, 2001.

Grenfell, T. C. and Warren, S. G.: Representation of a nonspherical ice particle by a collection of independent
spheres for scattering and absorption of radiation, Journal of Geophysical Research: Atmospheres, 104, 31 697–31 709,
570   https://doi.org/https://doi.org/10.1029/1999JD900496, 1999.

Hale, G. M. and Querry, M. R.: Optical Constants of Water in the 200-nm to 200-μm Wavelength Region, Appl. Opt., 12, 555–563,
https://doi.org/10.1364/AO.12.000555, 1973.

Haynes, J. M., L'Ecuyer, T. S., Stephens, G. L., and Jakob, C.: Cloud and precipitation regimes revealed by combined CloudSat and ISCCP
observations, AGU Fall Meeting Abstracts, 44, 04, http://adsabs.harvard.edu/abs/2009AGUFM.A44B..04H, 2009.

575 Hogan, R. J. and Westbrook, C. D.: Equation for the Microwave Backscatter Cross Section of Aggregate Snowflakes Using the Self-Similar Rayleigh-Gans Approximation, Journal of the Atmospheric Sciences, 71, 3292–3301, https://doi.org/10.1175/JAS-D-13-0347.1, 2014.

Hogan, R. J., Honeyager, R., Tyynelä, J., and Kneifel, S.: Calculating the millimetre-wave scattering phase function of snowflakes using the self-similar Rayleigh-Gans Approximation, Quarterly Journal of the Royal Meteorological Society, 143, 834–844, https://doi.org/10.1002/qj.2968, 2017.

580 Hollstein, A. and Fischer, J.: Radiative transfer solutions for coupled atmosphere ocean systems using the matrix operator technique, Journal of Quantitative Spectroscopy and Radiative Transfer, 113, 536–548, https://doi.org/https://doi.org/10.1016/j.jqsrt.2012.01.010, 2012.

Hostetler, C. A., Behrenfeld, M. J., Hu, Y., Hair, J. W., and Schulien, J. A.: Spaceborne Lidar in the Study of Marine Systems, Annual Review of Marine Science, 10, 121–147, https://doi.org/10.1146/annurev-marine-121916-063335, pMID: 28961071, 2018.

Illingworth, A. J., Barker, H. W., Beljaars, A., Ceccaldi, M., Chepfer, H., Clerbaux, N., Cole, J., Delanoë, J., Domenech, C., Donovan, D. P.,
585 Fukuda, S., Hirakata, M., Hogan, R. J., Huenerbein, A., Kollias, P., Kubota, T., Nakajima, T., Nakajima, T. Y., Nishizawa, T., Ohno, Y., Okamoto, H., Oki, R., Sato, K., Satoh, M., Shephard, M. W., Velázquez-Blázquez, A., Wandinger, U., Wehr, T., and van Zadelhoff, G.-J.: The EarthCARE Satellite: The Next Step Forward in Global Measurements of Clouds, Aerosols, Precipitation, and Radiation, Bulletin of the American Meteorological Society, 96, 1311–1332, https://doi.org/10.1175/BAMS-D-12-00227.1, 2015.

Inness, A., Ades, M., Agustí-Panareda, A., Barré, J., Benedictow, A., Blechschmidt, A.-M., Dominguez, J. J., Engelen, R., Eskes, H., Flem-
590 ming, J., Huijnen, V., Jones, L., Kipling, Z., Massart, S., Parrington, M., Peuch, V.-H., Razinger, M., Remy, S., Schulz, M., and Suttie, M.: The CAMS reanalysis of atmospheric composition, Atmospheric Chemistry and Physics, 19, 3515–3556, https://doi.org/10.5194/acp-19-3515-2019, 2019.

Josset, D., Tanelli, S., Hu, Y., Pelon, J., and Zhai, P.: Analysis of Water Vapor Correction for CloudSat W-Band Radar, IEEE Transactions on Geoscience and Remote Sensing, 51, 3812–3825, https://doi.org/10.1109/TGRS.2012.2228659, 2013.

595 Kato, S., Ackerman, T. P., Mather, J. H., and Clothiaux, E. E.: The k-distribution method and correlated-k approximation for a shortwave radiative transfer model, Journal of Quantitative Spectroscopy and Radiative Transfer, 62, 109–121, https://doi.org/https://doi.org/10.1016/S0022-4073(98)00075-2, 1999.

Kollias, P., Clothiaux, E. E., Miller, M. A., Albrecht, B. A., Stephens, G. L., and Ackerman, T. P.: Millimeter-Wavelength Radars: New Frontier in Atmospheric Cloud and Precipitation Research, Bull. Amer. Meteorol. Soc., 88, 1608–1624, https://doi.org/10.1175/BAMS-
600 88-10-1608, 2007.

Kollias, P., Tanelli, S., Battaglia, A., and Tatarevic, A.: Evaluation of EarthCARE Cloud Profiling Radar Doppler Velocity Measurements in Particle Sedimentation Regimes, Journal of Atmospheric and Oceanic Technology, 31, 366–386, https://doi.org/10.1175/JTECH-D-11-00202.1, 2014.

Kollias, P., Battaglia, A., Lamer, K., Treserras, B. P., and Braun, S. A.: Mind the Gap - Part 3: Doppler Velocity Measurements From Space,
605 Frontiers in Remote Sensing, 3, https://doi.org/10.3389/frsen.2022.860284, 2022a.

Kollias, P., Puidgomènech Treserras, B., Battaglia, A., Borque, P., and Tatarevic, A.: Processing reflectivity and Doppler velocity from EarthCARE's cloud profiling radar: the C-FMR, C-CD and C-APC products, EGUsphere, 2022, 1–25, https://doi.org/10.5194/egusphere-2022-1284, 2022b.

Lamer, K., Kollias, P., Battaglia, A., and Preval, S.: Mind the gap – Part 1: Accurately locating warm marine boundary layer clouds and
610 precipitation using spaceborne radars, Atmospheric Measurement Techniques, 13, 2363–2379, https://doi.org/10.5194/amt-13-2363-2020, 2020.

Li, J., Huang, J., Stamnes, K., Wang, T., Lv, Q., and Jin, H.: A global survey of cloud overlap based on CALIPSO and CloudSat measurements, Atmospheric Chemistry and Physics, 15, 519–536, https://doi.org/10.5194/acp-15-519-2015, 2015.

Lin, Z., Stamnes, S. A., Jin, Z., Laszlo, I., Tsay, S.-C., Wiscombe, W. J., and Stamnes, K.: Improved discrete ordinate solutions in the presence of an anisotropically reflecting lower boundary: Upgrades of the DISORT computational tool, Journal of Quantitative Spectroscopy & Radiative Transfer, 157, 119–134, 2015.

Miles, R. B., Lempert, W. R., and Forkey, J. N.: Laser Rayleigh scattering, Measurement Science and Technology, 12, R33–R51, https://doi.org/10.1088/0957-0233/12/5/201, 2001.

Mitchell, D. L. and Heymsfield, A. J.: Refinements in the Treatment of Ice Particle Terminal Velocities, Highlighting Aggregates, Journal of the Atmospheric Sciences, 62, 1637–1644, https://doi.org/10.1175/JAS3413.1, 2005.

Moody, E. G., King, M. D., Schaaf, C. B., Hall, D. K., and Platnick, S.: Northern Hemisphere five-year average (2000–2004) spectral albedos of surfaces in the presence of snow: Statistics computed from Terra MODIS land products, Remote Sensing of Environment, 111, 337–345, https://doi.org/https://doi.org/10.1016/j.rse.2007.03.026, remote Sensing of the Cryosphere Special Issue, 2007.

Pan, X., Shneider, M. N., and Miles, R. B.: Coherent Rayleigh-Brillouin Scattering, Phys. Rev. Lett., 89, 183 001, https://doi.org/10.1103/PhysRevLett.89.183001, 2002.

Qu, Z., Donovan, D. P., Barker, H. W., Cole, J. N. S., and Shephard, M.: High-resolution NWP model simulations in support of EarthCARE retrieval algorithm development studies, Atmospheric Measurement Techniques, to be submitted, 2022.

Rosenkranz, P. W.: Water vapor microwave continuum absorption: A comparison of measurements and models, Radio Science, 33, 919–928, https://doi.org/https://doi.org/10.1029/98RS01182, 1998.

Saleh, B. E. A. and Teich, M. C.: Fundamentals of photonics; 1st ed., Wiley, New York, NY, https://cds.cern.ch/record/244535, 1991.

Schaaf, C. B., Gao, F., Strahler, A. H., Lucht, W., Li, X., Tsang, T., Strugnell, N. C., Zhang, X., Jin, Y., Muller, J.-P., Lewis, P., Barnsley, M., Hobson, P., Disney, M., Roberts, G., Dunderdale, M., Doll, C., d'Entremont, R. P., Hu, B., Liang, S., Privette, J. L., and Roy, D.: First operational BRDF, albedo nadir reflectance products from MODIS, Remote Sensing of Environment, 83, 135–148, https://doi.org/https://doi.org/10.1016/S0034-4257(02)00091-3, the Moderate Resolution Imaging Spectroradiometer (MODIS): a new generation of Land Surface Monitoring, 2002.

Tanelli, S., Durden, S. L., Im, E., Pak, K. S., Reinke, D. G., Partain, P., Haynes, J. M., and Marchand, R. T.: CloudSat's cloud profiling radar after two years in orbit: performance, calibration, and processing, IEEE Transactions on Geoscience and Remote Sensing, 46, 3560–3573, https://doi.org/10.1109/TGRS.2008.2002030, 2008.

Velázquez-Blázquez, A., Baudrez, E., Clerbaux, N., and Domenech, C.: Unfiltering of the EarthCARE Broadband Radiometer (BBR) observations: the BM-RAD product, Atmospheric Measurement Techniques, to be submitted, 2022.

Vidot, J. and Borbáas, E.: Land surface VIS/NIR BRDF atlas for RTTOV-11: model and validation against SEVIRI land SAF albedo product, Quarterly Journal of the Royal Meteorological Society, 140, https://doi.org/10.1002/qj.2288, 2014.

Wandinger, U., Floutsi, A., Baars, H., Haarig, M., Hünerbein, A., Docter, N., Donovan, D., and van Zadelhoff, G.-J.: HETEAC – The Hybrid End-To-End Aerosol Classification model for EarthCARE, Atmospheric Measurement Techniques, to be submitted, 2022.

Zhou, C. and Yang, P.: Backscattering peak of ice cloud particles, Opt. Express, 23, 11 995–12 003, https://doi.org/10.1364/OE.23.011995, 2015.

Zrnic, D. S.: Simulation of weatherlike Doppler spectra and signal, J. Appl. Meteorol., 14, 619–620, 1975.

Zrnic, D. S.: Spectral moment estimates from correlated pulse pairs, IEEE Trans. Aerosp. Electron. Syst., AES-13, 344–354, 1977.